IMA Journal of Applied Mathematics (2020) **85**, 421–466
doi:10.1093/imamat/hxaa011
Advance Access publication on 30 April 2020

High-contrast approximation for penetrable wedge diffraction

M. A. Nethercote* and R. C. Assier
School of Mathematics, University of Manchester, Oxford Road, Manchester M13 9PL, UK
*Corresponding author: matthew.nethercote@manchester.ac.uk

and

I. D. Abrahams
Isaac Newton Institute, University of Cambridge, 20 Clarkson Road, Cambridge CB3 0EH, UK

[Received on 13 August 2019; revised on 22 January 2020; accepted on 6 March 2020]

The important open canonical problem of wave diffraction by a penetrable wedge is considered in the high-contrast limit. Mathematically, this means that the contrast parameter, the ratio of a specific material property of the host and the wedge scatterer, is assumed small. The relevant material property depends on the physical context and is different for acoustic and electromagnetic waves for example. Based on this assumption, a new asymptotic iterative scheme is constructed. The solution to the penetrable wedge is written in terms of infinitely many solutions to (possibly inhomogeneous) impenetrable wedge problems. Each impenetrable problem is solved using a combination of the Sommerfeld–Malyuzhinets and Wiener–Hopf techniques. The resulting approximated solution to the penetrable wedge involves a large number of nested complex integrals and is hence difficult to evaluate numerically. In order to address this issue, a subtle method (combining asymptotics, interpolation and complex analysis) is developed and implemented, leading to a fast and efficient numerical evaluation. This asymptotic scheme is shown to have excellent convergent properties and leads to a clear improvement on extant approaches.

Keywords: wave diffraction, penetrable wedge.

1. Introduction

Waves diffraction by edges, wedges and ledges has been studied in numerous physical contexts (acoustics, elasticity, electromagnetism) by many distinguished scientists. Its rigorous mathematical treatment was established in the late 19th century thanks to Sommerfeld who solved the famous half-plane problem (Sommerfeld, 1896) (for the English translation, see Sommerfeld, 2003) and later conceived the first solution that models impenetrable wedge diffraction (with the wedge being a rational multiple of π) using the method of images (Sommerfeld, 1901). This topic has remained an active and productive area of research ever since.

Macdonald was the first to solve impenetrable wedge problems with arbitrary wedge angles (Macdonald, 1902). In this paper, he considered an incident line source and obtained a series solution before converting it into an integral form similar to that conceived by Sommerfeld (commonly known as Sommerfeld integrals) and provided the solution for an incident plane wave.

Since then, several ingenious mathematical procedures have been developed to tackle diffraction problems. These include the Wiener–Hopf technique (Wiener & Hopf, 1931; Noble, 1958; Lawrie & Abrahams, 2007), the Sommerfeld–Malyuzhinets technique (Malyuzhinets, 1958a,b; Babich *et al.*, 2007) and the Kontorovich–Lebedev transform (Kontorovich & Lebedev, 1939). Several asymptotic techniques have also been developed, including Keller's geometrical theory of diffraction

© The Author(s) 2020. Published by Oxford University Press on behalf of the Institute of Mathematics and its Applications. This is an Open Access article distributed under the terms of the Creative Commons Attribution License (http://creativecommons.org/licenses/by/4.0/), which permits unrestricted reuse, distribution, and reproduction in any medium, provided the original work is properly cited.

Downloaded from https://academic.oup.com/imamat/article/85/3/421/5822762 by University of Cambridge user on 21 September 2020

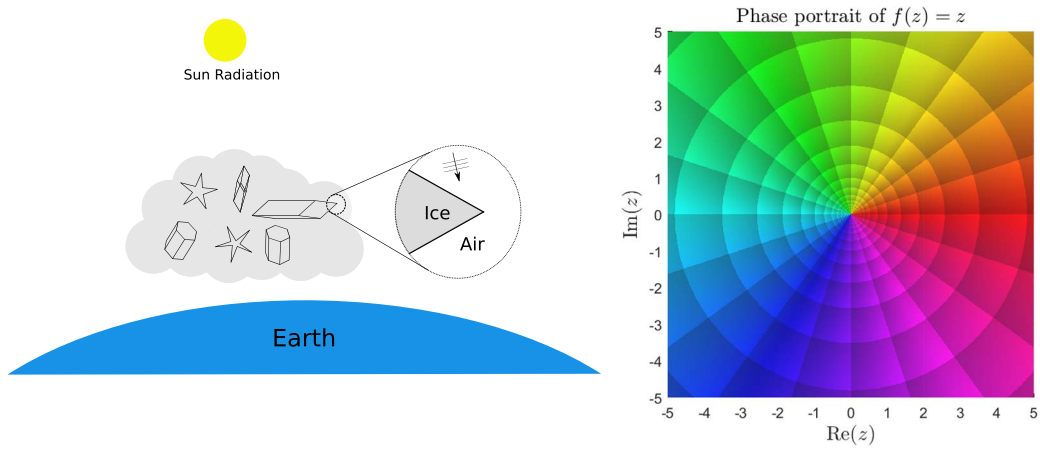

FIG. 1. Diagram outlining the application to ice crystal diffraction (left). The phase portrait of an identity map ($f(z) = z$) that assigns colours to the complex argument of f (right). For example, red will imply that $\arg(f) = 0$, green indicates $\arg(f) = \pi/2$, cyan indicates $\arg(f) = \pm\pi$ and so on.

(Keller, 1962), the uniform geometrical theory of diffraction (Kouyoumjian & Pathak, 1974) as well as the physical theory of diffraction (Ufimtsev, 2014) developed from Kirchhoff's approximation (Kirchhoff, 1883). Many of these techniques have been successfully applied to impenetrable wedge diffraction (see Nethercote *et al.*, 2020 for a review of these methods). It is also worth mentioning the important research undertaken for wedges subjected to impedance boundary condition (Malyuzhinets, 1958a; Senior, 1959; Williams, 1959; Daniele & Lombardi, 2006) or elastic wedges (Knopoff, 1969; Budaev & Bogy, 1998; Croisille & Lebeau, 1999).

Despite such progress, a clear analytical solution remains to be found for some wedge diffraction problems. This is the case for the penetrable wedge.

As one of the building blocks of the geometrical theory of diffraction, a full analytical solution to this problem would have a major impact on diffraction theory. For example, this would permit to approximate accurately and rapidly the fields diffracted by complicated structures such as penetrable truncated wedges or polygons subject to high frequency incident waves. Physical applications include noise transmission in non-viscous fluids, antenna theory and seismology.

Our initial interest in this problem was however triggered by another application related to climate modelling, that of light diffraction by ice crystals within clouds (transparent scatterers with sharp features, see Fig. 1, left). Such effect is one of the big uncertainties when calculating the Earth radiation budget, which feeds directly into climate change models (Smith *et al.*, 2015).

This application also motivated Groth *et al.* (2015, 2018) to extend the work by Chandler-Wilde *et al.* (2012) (dedicated to impenetrable scatterers) to combine the strengths of numerical and asymptotic schemes to produce an accurate approximation to the problem of diffraction by penetrable convex polygons (which could represent ice crystals for example). This technique, known as hybrid numerical-asymptotic, is based on enriching the basis functions used in the boundary element method in an educated way, inspired by exact solutions to canonical diffraction problems. The aim is to create numerical methods that do not become overly expensive at high frequency. It is acknowledged by these authors that the choice of basis functions in the penetrable case is not yet optimal and could be improved tremendously with a better understanding of the penetrable wedge problem.

Downloaded from https://academic.oup.com/imamat/article/85/3/421/5822762 by University of Cambridge user on 21 September 2020

Over the past few decades, there have been numerous attempts to find computational and/or asymptotic solutions to penetrable wedge problems.

Rawlins looked at the electromagnetic penetrable wedge case where the refractive index is close to unity. In Rawlins (1977, 1999), he considered an electromagnetic incident plane wave and reduced the problem to Fredholm integral equations of the second kind using either Green's second identity or the Kontorovich–Lebedev transform and a Neumann-type perturbation series. The result of Rawlins (1999) is a formula that is simple and fast to implement. However, this particular limit of unit refractive index is not particularly suited to the applications we have in mind, and, as acknowledged by the author, the method developed can be difficult to extend to higher orders.

Budaev & Bogy (1999) looked at finding the acoustic pressure field for a special case of penetrable wedge diffraction. Relying on previous papers on Rayleigh wave scattering by elastic wedges (Budaev & Bogy, 1995, 1996, 1998), they designed the problem symmetrically with an antisymmetric incident field so that they could formulate it on a half-space domain. They derived a system of difference equations that were solved via singular integral operators and a Neumann series using the assumptions that the host wedge region is very thin and the ratio of densities is close to unity.

We should also note some recent approaches using simple layer potentials discussed in Croisille & Lebeau (1999) for elastic wedge diffraction. These ideas highly influenced the research by Mokeeva on the well-posedness of the penetrable wedge problem (Mokeeva, 2006, 2007). Alongside Babich, she would show the uniqueness of the problem (Babich & Mokeeva, 2008) and would later develop a numerical solution of these simple layer potentials (Babich *et al.*, 2012).

More related to the physical assumptions of the present paper, there is an earlier attempt to create a high-contrast asymptotic approximation. Lyalinov (1999) uses the Sommerfeld–Malyuzhinets technique and asymptotically approximates the spectral functions assuming high contrast between the material of the wedge and that of the host. The result is a leading order uniform asymptotic formula that is very fast to evaluate. The advantages and inconveniences of this approach will be discussed when comparing it to our results.

Shanin (1996, 1998) looks at solving wedge problems with inhomogeneous impedance boundary conditions via the Wiener–Hopf technique. He first considers the case where the angular domain containing the total wave field has an interior angle less than π. He later extends the method to angles exceeding π and applies a reflection method to a special case where the angle is rational of the form π/m. This method was key to showing the Wiener–Hopf technique capability to be applied to wedge problems and, as we will see, it can be extended to the penetrable wedge.

Building on their previous work (Daniele, 2003a,b, 2010, 2011) and (Daniele & Lombardi, 2006, 2007), Daniele & Lombardi (2011) have adapted the Wiener–Hopf technique to electromagnetic wave diffraction by penetrable wedges. This is achieved through a combination of multiple complex mappings, Fredholm factorization and analytical continuation via functional difference equations. Quadrature schemes are used to solve the resulting Fredholm integral equations and numerical results are given for four representative test cases. The authors have more recently begun to extend this method to more complex geometries such as a composition of wedges and slabs (Daniele *et al.*, 2017a,b,c, 2018).

Finally, it should be noted that Radlow (1964) adapted his ideas of two-complex variables Wiener–Hopf technique to the right-angled penetrable wedge and claimed to have found an analytic closed-form solution, though his solution was shown to be erroneous by Kraut & Lehman (1969). Functions of several complex variables are nevertheless a promising avenue in diffraction theory and have recently been exploited in Assier & Shanin (2019) and Assier & Abrahams (2019) for example.

Downloaded from https://academic.oup.com/imamat/article/85/3/421/5822762 by University of Cambridge user on 21 September 2020

In the present work, we propose an asymptotic scheme to solve the penetrable wedge problem, based on a high-contrast assumption. Throughout this article, we will rely on the knowledge of the locations of singularities and branch cuts of complex functions. In order for it to be simpler, we shall use MATLAB to visualize such functions in the style of Wegert (2012), using complex phase portraits. These plots of a complex function's argument allow for an easy and instantaneous visualization of the location and nature of the function's singularities. The right side of Fig. 1 is a phase portrait of $f(z) = z$ that we will refer to as a colour reference.

We start by formulating the penetrable wedge diffraction problem in Section 2 and define two separate regions, the host and the scatterer, and their respective wave fields connected at the wedge faces. The high-contrast assumption is made and its physical meaning is discussed. This allows us to design a high-contrast iterative scheme in Section 3 that splits the penetrable wedge problem into an infinite number of impenetrable wedge problems that can be dealt with separately.

In Section 4, following the methods developed by Shanin (1996), Daniele (2003b) and Nethercote *et al.* (2020), each impenetrable wedge problem is solved, leading to a closed-form solution in terms of nested integrals. As a proof of concept for our asymptotic expansion method, we apply it to the simple case where the wedge has opened up to create a half-space, for which an exact solution is known.

In Section 5, we discuss the numerical strategies used to evaluate the nested integrals. This is done by a subtle combination of interpolation, asymptotic analysis and analytic continuation via functional difference equations that leads to an efficient approximation of the host and scatterer wave fields for sufficiently high contrast. We study the convergence and the speed of our method and compare our results to the existing literature, showing clear improvements.

The appendices discuss the derivation of an important complex mapping that is used to link the wave fields in spectral space as well as some asymptotic analysis of the integral solutions.

2. Problem formulation

The problem we are considering is the diffraction of a plane wave normally incident on an infinite penetrable wedge. We assume that the problem is time harmonic with time factor $e^{-i\omega t}$, where ω is the frequency, allowing us to reduce the linear wave equation to the Helmholtz equation and work in the frequency domain. We define Ω_1 (resp. Ω_2) to be the region outside (resp. inside) the wedge scatterer. These two angular domains have two different sets of material parameters, i.e. density ($\rho_{1,2}$), magnetic permeability ($\mu_{1,2}$) or electric permittivity ($\epsilon_{1,2}$). There will also be different wave speeds ($c_{1,2}$) and different wavenumbers ($k_{1,2}$) that satisfy $\omega = c_1 k_1 = c_2 k_2$. For simplicity, we shall assume that the wave parameters are independent of the material parameters. The angular domains will have the following definitions:

$$\Omega_1 = \left\{(r,\theta) : r > 0,\ -\theta_{\mathrm{w}} < \theta < \theta_{\mathrm{w}}\right\}, \quad \Omega_2 = \left\{(r,\theta) : r > 0,\ \theta_{\mathrm{w}} < \theta < 2\pi - \theta_{\mathrm{w}}\right\}, \tag{2.1}$$

where $0 < \theta_{\mathrm{w}} < \pi$. Defining $\bar{\theta}_{\mathrm{w}} = \pi - \theta_{\mathrm{w}}$, the interior angle of the wedge scatterer is $2\bar{\theta}_{\mathrm{w}}$, as illustrated in Fig. 2.

Let the total wave solutions in Ω_1 and Ω_2 be called Φ and Ψ, respectively. In an acoustic setting, Φ and Ψ represent pressure fields whereas in an electromagnetic setting, they represent either the electric or magnetic field components parallel to the wedge edge (depending on the polarization of the incident

Downloaded from https://academic.oup.com/imamat/article/85/3/421/5822762 by University of Cambridge user on 21 September 2020

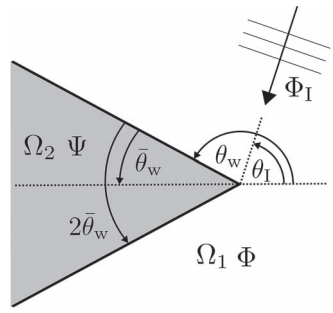

FIG. 2. The geometry of the problem where the white region is the host (Ω_1), the grey region is the wedge scatterer (Ω_2) and Φ_I is the incident plane wave.

wave). These two solutions satisfy the homogeneous Helmholtz equation with wavenumbers k_1 and k_2 respectively,

$$\nabla^2\Phi + k_1^2\Phi = 0, \text{ in } \Omega_1, \tag{2.2}$$

$$\nabla^2\Psi + k_2^2\Psi = 0, \text{ in } \Omega_2. \tag{2.3}$$

At the two wedge faces $\theta = \pm\theta_w$, Φ and Ψ must satisfy the following interface conditions:

$$\text{Top face: } \Phi|_{\theta=\theta_w} = \Psi|_{\theta=\pi-\bar{\theta}_w}, \quad \left.\frac{\partial\Phi}{\partial\theta}\right|_{\theta=\theta_w} = \lambda \left.\frac{\partial\Psi}{\partial\theta}\right|_{\theta=\pi-\bar{\theta}_w}, \tag{2.4}$$

$$\text{Bottom face: } \Phi|_{\theta=-\theta_w} = \Psi|_{\theta=\pi+\bar{\theta}_w}, \quad \left.\frac{\partial\Phi}{\partial\theta}\right|_{\theta=-\theta_w} = \lambda \left.\frac{\partial\Psi}{\partial\theta}\right|_{\theta=\pi+\bar{\theta}_w}, \tag{2.5}$$

where the contrast parameter λ is defined as,

$$\lambda = \frac{\rho_1}{\rho_2}, \ \frac{\mu_1}{\mu_2} \text{ or } \frac{\epsilon_1}{\epsilon_2} \tag{2.6}$$

in the acoustic, electric polarized and magnetic polarized cases, respectively. For an acoustic setting, these interface conditions will ensure the continuity of the pressure and the normal velocity across the wedge faces. In an electromagnetic setting, the interface conditions will ensure the continuity of tangential electromagnetic field components across the wedge faces. In this paper, we consider λ to be a small, positive parameter ($\lambda \ll 1$).

The incident wave (illustrated in Fig. 2 as Φ_I) is a unit-amplitude plane wave with wavenumber k_1 and incident angle θ_I. This incident wave satisfies (2.2) but not (2.3) so it is a component of the host wave field Φ only,

$$\Phi_I = e^{-ik_1 r\cos(\theta-\theta_I)}, \ (r,\theta) \in \Omega_1, \ \theta_I \in [0,\theta_w], \tag{2.7}$$

where we say $\theta_I \geq 0$ for convenience due to the symmetry of the problem.

Both the total wave solutions can be decomposed into geometrical-optic (GO) and diffracted (Diff) wave components. The GO components, Φ_{GO} and Ψ_{GO}, contain the incident wave and all reflected and

Downloaded from https://academic.oup.com/imamat/article/85/3/421/5822762 by University of Cambridge user on 21 September 2020

transmitted waves produced by the wedge scatterer. The remaining diffracted wave components, Φ_{Diff} and Ψ_{Diff}, satisfy the 2D Sommerfeld-radiation condition that we write in integral form:

$$\lim_{r\to\infty}\int_{-\theta_{\text{w}}}^{\theta_{\text{w}}}\left|\frac{\partial\Phi_{\text{Diff}}}{\partial r}-ik_1\Phi_{\text{Diff}}\right|^2 r\mathrm{d}\theta=0\quad\text{and}\quad\lim_{r\to\infty}\int_{\pi-\bar{\theta}_{\text{w}}}^{\pi+\bar{\theta}_{\text{w}}}\left|\frac{\partial\Psi_{\text{Diff}}}{\partial r}-ik_2\Psi_{\text{Diff}}\right|^2 r\mathrm{d}\theta=0. \tag{2.8}$$

Lastly, we will have edge conditions at the origin. These are obtained using the Frobenius method (see, e.g. Bender & Orszag, 1999 for a good treatise on the method) on the Helmholtz equation, resulting in the following asymptotic approximation as $r\to 0$:

$$\Phi(r,\theta)\underset{r\to 0}{\sim}\mathcal{A}+\left[\mathcal{B}_1\cos(\widehat{\delta}\theta)+\mathcal{B}_2\sin(\widehat{\delta}\theta)\right]r^{\widehat{\delta}}-\frac{\mathcal{A}}{4}(k_1r)^2+\ldots, \tag{2.9}$$

$$\Psi(r,\theta)\underset{r\to 0}{\sim}\mathcal{A}+\left[\mathcal{B}_3\cos(\widehat{\delta}\theta)+\mathcal{B}_4\sin(\widehat{\delta}\theta)\right]r^{\widehat{\delta}}-\frac{\mathcal{A}}{4}(k_2r)^2+\ldots, \tag{2.10}$$

where $\widehat{\delta}>0$. After applying the boundary conditions, (2.4) and (2.5), we find that $\widehat{\delta}$ must satisfy

$$(\cot(\widehat{\delta}\theta_{\text{w}})+\lambda\cot(\widehat{\delta}\bar{\theta}_{\text{w}}))(\cot(\widehat{\delta}\bar{\theta}_{\text{w}})+\lambda\cot(\widehat{\delta}\theta_{\text{w}}))=0. \tag{2.11}$$

To be consistent with the impenetrable wedge problem with Neumann boundary conditions ($\lambda=0$), we require that $\widehat{\delta}$ tends to $\delta=\frac{\pi}{2\theta_{\text{w}}}$ continuously as $\lambda\to 0$. This implies that the corresponding factor of (2.11) should remain zero,

$$\cot(\widehat{\delta}\theta_{\text{w}})+\lambda\cot(\widehat{\delta}\bar{\theta}_{\text{w}})=0. \tag{2.12}$$

We can hence Taylor expand $\widehat{\delta}$ about $\lambda=0$ to get,

$$\widehat{\delta}=\delta-\frac{\lambda}{\theta_{\text{w}}}\tan(\delta\pi)+O(\lambda^2), \tag{2.13}$$

which suggests that the singularity is 'weaker' than the impenetrable wedge case when $\theta_{\text{w}}>\pi/2$ because

$$\tan(\delta\pi)<0,\quad\text{for all }\theta_{\text{w}}\in\left(\frac{\pi}{2},\pi\right). \tag{2.14}$$

This statement is supported by Table 5.1 in Van Bladel (2006), which is a table of values for $\hat{\delta}$ with respect to λ and θ_{w}. This means that we define the edge conditions to be,

$$\Phi,\Psi\underset{r\to 0}{\sim}\mathcal{A}+O\left(r^{\min(\widehat{\delta},2)}\right), \tag{2.15}$$

Downloaded from https://academic.oup.com/imamat/article/85/3/421/5822762 by University of Cambridge user on 21 September 2020

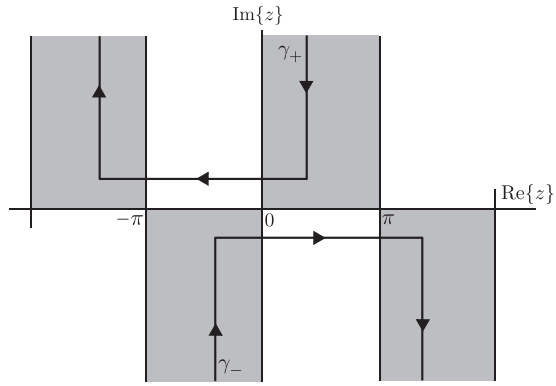

FIG. 3. The Sommerfeld contours are $\gamma_\pm$ and the grey half-strips are where the Sommerfeld integrand rapidly decays.

where $\mathcal{A}$ is constant. We seek solutions to the Helmholtz equation in Sommerfeld integral form,

$$\Phi(r,\theta) = \frac{1}{2\pi i}\int_{\gamma_+ + \gamma_-} e^{-ik_1 r\cos(z)} s(\theta+z)\mathrm{d}z = \frac{1}{2\pi i}\int_{\gamma_+} e^{-ik_1 r\cos(z)}\left[s(\theta+z) - s(\theta-z)\right]\mathrm{d}z, \quad (2.16)$$

$$\Psi(r,\theta) = \frac{1}{2\pi i}\int_{\gamma_+ + \gamma_-} e^{-ik_2 r\cos(z)} q(\theta-\pi+z)\mathrm{d}z = \frac{1}{2\pi i}\int_{\gamma_+} e^{-ik_2 r\cos(z)}\left[q(\theta-\pi+z) - q(\theta-\pi-z)\right]\mathrm{d}z, \quad (2.17)$$

where γ_+ and γ_- are known as the Sommerfeld contours (illustrated in Fig. 3), and the spectral functions $s(z)$ and $q(z)$ are the unknowns to be determined.

These Sommerfeld integrals automatically satisfy the relevant Helmholtz equation and the arrangement of the spectral functions is necessary for the diffracted wave to satisfy the relevant radiation condition (the details are omitted here but thorough explanations can be found in these useful textbooks (Sommerfeld, 1954; Bowman *et al.*, 1987) and Babich *et al.* (2007)).

Since the exponentials in the two Sommerfeld integrals (2.16) and (2.17) have different wavenumbers, we will need to derive a mapping $g(z)$ and associated inverse $h(z)$ from the following identities:

$$k_2\cos(g(z)) = k_1\cos(z), \quad k_1\cos(h(z)) = k_2\cos(z), \quad (2.18)$$

in order to write the two Sommerfeld integrals as one. Note that these mappings have been used before by a number of authors in a wedge context (Larsen, 1981; Budaev, 1995; Lyalinov, 1999; Daniele, 2011). Both of these mappings have an infinite number of branch cuts that need to be defined in a very specific way. They also satisfy the following set of properties:

- $f(-z) = -f(z)$,
- $f(z^*) = (f(z))^*$ where z^* is the complex conjugate of z,
- $f(z+n\pi) = f(z) + n\pi$, for all $n \in \mathbb{Z}$,
- $f(z) \sim z$ as $\mathrm{Im}\{z\} \to \pm\infty$,

Downloaded from https://academic.oup.com/imamat/article/85/3/421/5822762 by University of Cambridge user on 21 September 2020

where f can be either g or h. Following the constructive procedure detailed in Appendix A, we obtain the following form of $g(z)$ and $h(z)$, where $\lambda_k = k_1/k_2 \in [0, 1]$:

$$g(z) = z - i\ln(ie^{-iz}) + i\ln\left(i\lambda_k\cos(z) - i\left(i\lambda_k\sin(z) - (1-\lambda_k^2)^{\frac{1}{2}}\right)^{\frac{1}{2}}\left(i\lambda_k\sin(z) + (1-\lambda_k^2)^{\frac{1}{2}}\right)^{\frac{1}{2}}\right), \tag{2.19}$$

$$h(z) = z - i\ln(ie^{-iz}) - i\ln(\lambda_k) + i\ln\left(i\cos(z) + \left(\sin(z) - (1-\lambda_k^2)^{\frac{1}{2}}\right)^{\frac{1}{2}}\left(\sin(z) + (1-\lambda_k^2)^{\frac{1}{2}}\right)^{\frac{1}{2}}\right). \tag{2.20}$$

The individual square roots are defined by (A.5) and (A.7) for $g(z)$ and $h(z)$, respectively. It is worthwhile to note that we choose $\lambda_k \in [0, 1]$ for brevity and to stay consistent with λ being small. If $\lambda_k > 1$, then $g(z)$ and $h(z)$ will swap their branch cut definitions (detailed in Appendix A). Overall, this will not alter the methodology in this article; however, minor adaptations to deal with this case should be considered in Section 5.

Both these definitions satisfy all of the required conditions including them being the inverse of each other. It will be useful later to state the derivatives of $g(z)$ and $h(z)$ implicitly,

$$g'(z) = \frac{\lambda_k\sin(z)}{\sin(g(z))}, \quad h'(z) = \frac{\sin(z)}{\lambda_k\sin(h(z))}, \tag{2.21}$$

and note the asymptotic expansions of $g(z)$ and $h(z)$ as $\mathrm{Im}\{z\} \to \pm\infty$,

$$g(z) = z \pm i\ln(\lambda_k) \mp \frac{i(1-\lambda_k^2)}{\lambda_k^2}e^{\pm 2iz} + O\left(e^{\pm 4iz}\right), \tag{2.22}$$

$$h(z) = z \mp i\ln(\lambda_k) \pm i(1-\lambda_k^2)e^{\pm 2iz} + O\left(e^{\pm 4iz}\right). \tag{2.23}$$

As an example, Fig. 4 illustrates a phase portrait of (2.19) and (2.20) evaluated by MATLAB, where $\lambda_k = 1/2$.

3. High-contrast approximation

We want to simplify the penetrable wedge problem by using a high-contrast ($\lambda \ll 1$) approximation. The idea being to decompose the 'difficult' penetrable problem into an infinite set of 'simpler' impenetrable ones. To this end, we pose the following asymptotic series:

$$\Phi = \Phi^{(0)} + \lambda\Phi^{(1)} + \lambda^2\Phi^{(2)} + O\left(\lambda^3\right), \tag{3.1}$$

$$\Psi = \Psi^{(0)} + \lambda\Psi^{(1)} + \lambda^2\Psi^{(2)} + O\left(\lambda^3\right). \tag{3.2}$$

Each of the components of (3.1) (respectively (3.2)) satisfy the Helmholtz equation and the radiation conditions with wavenumber k_1 (respectively k_2).

Downloaded from https://academic.oup.com/imamat/article/85/3/421/5822762 by University of Cambridge user on 21 September 2020

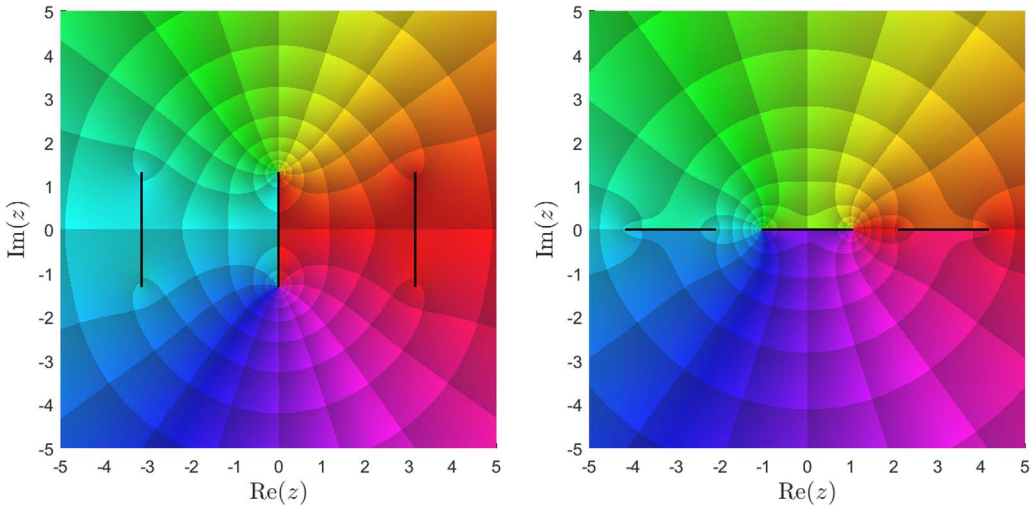

FIG. 4. Phase portraits of the mappings $g(z)$ (left) and $h(z)$ (right) by the formulae (2.19) and (2.20), respectively, where $\lambda_k = 1/2$. In these figures, the black lines represent branch cuts. See Fig. 1 (right) for colour reference.

It is important to understand how this high-contrast approximation affects the interface conditions. By substituting (3.1) and (3.2) into (2.4) and (2.5), then organizing with respect to λ, we obtain

$$\begin{gathered}\left(\Phi^{(0)}|_{\theta=\pm\theta_{\mathrm{w}}} - \Psi^{(0)}|_{\theta=\pi\mp\bar{\theta}_{\mathrm{w}}}\right) + \lambda\left(\Phi^{(1)}|_{\theta=\pm\theta_{\mathrm{w}}} - \Psi^{(1)}|_{\theta=\pi\mp\bar{\theta}_{\mathrm{w}}}\right) + \ldots = 0,\\ \left(\frac{\partial\Phi^{(0)}}{\partial\theta}\bigg|_{\theta=\pm\theta_{\mathrm{w}}}\right) + \lambda\left(\frac{\partial\Phi^{(1)}}{\partial\theta}\bigg|_{\theta=\pm\theta_{\mathrm{w}}} - \frac{\partial\Psi^{(0)}}{\partial\theta}\bigg|_{\theta=\pi\mp\bar{\theta}_{\mathrm{w}}}\right) + \ldots = 0.\end{gathered} \tag{3.3}$$

Each of these brackets must be identically equal to zero for the interface conditions to be satisfied. The first component, $\Phi^{(0)}$, will hence satisfy homogeneous Neumann boundary conditions and all others will satisfy inhomogeneous Dirichlet or Neumann boundary conditions where the forcing depends explicitly on the previously obtained component.

Since the incident plane wave has no dependence on λ and is only present in Ω_1, then it has no direct influence on any components other than $\Phi^{(0)}$. This means that the source of excitation for all other components are the forcing in the inhomogeneous boundary conditions.

The edge conditions (2.9)–(2.10) can also be split up among each of the components by Taylor expanding $\widehat{\delta}$ and $\mathcal{A}$ about $\lambda = 0$ (see section 5.3.1 in Nethercote, 2019 for more details). We can show that all components have the edge condition of the form,

$$\Phi^{(j)}, \Psi^{(j)} \underset{r\to 0}{\sim} \mathcal{A}^{(j)} + O\left(r^{\delta}(\ln(r))^{j}, r^{2}\right) + \ldots \text{ where } j = 0, 1, 2, \ldots. \tag{3.4}$$

Note that $O\left(r^{\delta}(\ln(r))^{j}, r^{2}\right)$ is equal to $O\left(r^{\delta}(\ln(r))^{j}\right)$ (respectively $O(r^2)$) when $\delta \leq 2$ (respectively $\delta > 2$). In this article, we shall assume that $\delta \leq 2$ for brevity. It is important to note that in the case where $\delta > 2$, the methodology and the final solution given in this article will remain the same, apart from replacing $O\left(r^{\delta}(\ln(r))^{j}, r^{2}\right)$ by $O\left(r^{2}\right)$ in the edge conditions.

Downloaded from https://academic.oup.com/imamat/article/85/3/421/5822762 by University of Cambridge user on 21 September 2020

Each of the problems for the high-contrast approximation components, $\Phi^{(j)}$ and $\Psi^{(j)}$ are independent of λ and hence create an iterative scheme to approximate the solution to the penetrable wedge problem.

The initial problem, call it $\mathcal{P}_{\Phi}^{(0)}$, is for the leading order component of the exterior solution, $\Phi^{(0)}$, defined in Ω_1.

$$\mathcal{P}_{\Phi}^{(0)}: \begin{cases} \nabla^2\Phi^{(0)} + k_1^2\Phi^{(0)} = 0 & \text{(Governing equation)} \quad (3.5a) \\ \left.\dfrac{\partial\Phi^{(0)}}{\partial\theta}\right|_{\theta=\pm\theta_{\mathrm{w}}} = 0 & \text{(Boundary conditions)} \quad (3.5b) \\ \Phi_{\mathrm{I}}^{(0)} = e^{-ik_1 r\cos(\theta-\theta_{\mathrm{I}})} & \text{(Plane wave forcing)} \quad (3.5c) \\ \lim\limits_{r\to\infty}\displaystyle\int_{-\theta_{\mathrm{w}}}^{\theta_{\mathrm{w}}}\left|\frac{\partial\Phi_{\mathrm{Diff}}^{(0)}}{\partial r} - ik_1\Phi_{\mathrm{Diff}}^{(0)}\right|^2 r\mathrm{d}\theta = 0 & \text{(Radiation condition)} \quad (3.5d) \\ \Phi^{(0)} \underset{r\to 0}{=} \mathcal{A}^{(0)} + O\left(r^{\delta}\right) & \text{(Edge condition)} \quad (3.5e) \end{cases}$$

$\mathcal{P}_{\Phi}^{(0)}$ is exactly the same as the impenetrable wedge problem with Neumann boundary conditions. The solution to this problem is stated in the form of a Sommerfeld integral,

$$\Phi^{(0)} = \frac{1}{2\pi i}\int_{\gamma_+} e^{-ik_1 r\cos(z)}\left[s^{(0)}(\theta+z) - s^{(0)}(\theta-z)\right]\mathrm{d}z, \tag{3.6}$$

where $s^{(0)}(z)$ is the unknown spectral function to find. The solution is well known and is solvable with numerous different methods (see Nethercote *et al.*, 2020). The resulting solution is,

$$s^{(0)}(z) = \frac{\delta\cos(\delta z)}{\sin(\delta z) - \sin(\delta\theta_{\mathrm{I}})}, \quad \text{where,} \quad \delta = \frac{\pi}{2\theta_{\mathrm{w}}}. \tag{3.7}$$

This spectral function has a few useful properties that will be reused later.

$$\text{Antisymmetry:} \quad s^{(0)}(\pm 2\theta_{\mathrm{w}} - z) = -s^{(0)}(z) \tag{3.8}$$

$$\text{Periodicity:} \quad s^{(0)}(4\theta_{\mathrm{w}} + z) = s^{(0)}(z) \tag{3.9}$$

$$\text{Conjugacy:} \quad s^{(0)}(z^*) = \left(s^{(0)}(z)\right)^*. \tag{3.10}$$

Lastly, we shall note the asymptotic series for $s^{(0)}(z)$ as $\mathrm{Im}\{z\} \to \pm\infty$,

$$s^{(0)}(z) = \mp i\delta - 2\delta\sin(\delta\theta_{\mathrm{I}})e^{\pm i\delta z} + O\left(e^{\pm 2i\delta z}\right). \tag{3.11}$$

All of the other components satisfy one of two types of problems. The first type, $\mathcal{P}_{\Psi}^{(j)}$ for $j = 0, 1, 2...$, is for the components of the interior solution $\Psi^{(j)}$ that are defined in Ω_2. This type has no incoming

Downloaded from https://academic.oup.com/imamat/article/85/3/421/5822762 by University of Cambridge user on 21 September 2020

plane waves and satisfies inhomogeneous Dirichlet boundary conditions depending on the known $\Phi^{(j)}$ component.

$$\mathcal{P}_{\Psi}^{(j)}:\begin{cases}\nabla^2\Psi^{(j)}+k_2^2\Psi^{(j)}=0 & \text{(Governing equation)} \quad (3.12a)\\ \Psi^{(j)}|_{\theta=\pi\mp\bar{\theta}_{\mathrm{w}}}=\Phi^{(j)}|_{\theta=\pm\theta_{\mathrm{w}}} & \text{(Boundary conditions)} \quad (3.12b)\\ \text{Not applicable here} & \text{(Plane wave forcing)} \quad (3.12c)\\ \lim\limits_{r\to\infty}\int_{\pi-\bar{\theta}_{\mathrm{w}}}^{\pi+\bar{\theta}_{\mathrm{w}}}\left|\dfrac{\partial\Psi_{\mathrm{Diff}}^{(j)}}{\partial r}-ik_2\Psi_{\mathrm{Diff}}^{(j)}\right|^2 r\mathrm{d}\theta=0 & \text{(Radiation condition)} \quad (3.12d)\\ \Psi^{(j)}\underset{r\to 0}{=}\mathcal{A}^{(j)}+O\left(r^{\delta}(\ln(r))^j\right) & \text{(Edge condition).} \quad (3.12e)\end{cases}$$

We seek a solution satisfying (3.12a) and (3.12d) in the form of (2.17),

$$\Psi^{(j)}=\frac{1}{2\pi i}\int_{\gamma_+}e^{-ik_2r\cos(z)}\left[q^{(j)}(\theta-\pi+z)-q^{(j)}(\theta-\pi-z)\right]\mathrm{d}z, \tag{3.13}$$

where, due to (3.12e), $q^{(j)}(z)$ has the following leading order behaviour as $\mathrm{Im}\{z\}\to\pm\infty$,[1]

$$q^{(j)}(z)=\pm A^{(j)}+O\left(z^je^{\pm i\delta z}\right) \tag{3.14}$$

with $A^{(j)}=-i\mathcal{A}^{(j)}/2$. A consequence of no incoming plane waves is that $q^{(j)}(z)$ has no poles in the strip,

$$\left\{z:-\bar{\theta}_{\mathrm{w}}<\mathrm{Re}\{z\}<\bar{\theta}_{\mathrm{w}}\right\}. \tag{3.15}$$

We apply the boundary conditions, (3.12b), to obtain,

$$\begin{aligned}\int_{\gamma_+}e^{-ik_2r\cos(z)}&\left[q^{(j)}(\mp\bar{\theta}_{\mathrm{w}}+z)-q^{(j)}(\mp\bar{\theta}_{\mathrm{w}}-z)\right]\mathrm{d}z\\ &=\int_{\gamma_+}e^{-ik_1r\cos(z)}\left[s^{(j)}(\pm\theta_{\mathrm{w}}+z)-s^{(j)}(\pm\theta_{\mathrm{w}}-z)\right]\mathrm{d}z.\end{aligned} \tag{3.16}$$

From (2.20), we apply the mapping $h(z)$ to transform the right integral and match the two exponentials. The mapped Sommerfeld contour can be deformed back to the original so that the two integrals are combined to produce,

$$\begin{aligned}\int_{\gamma_+}e^{-ik_2r\cos(z)}\Big[&q^{(j)}(\mp\bar{\theta}_{\mathrm{w}}+z)-q^{(j)}(\mp\bar{\theta}_{\mathrm{w}}-z)\\ &-h'(z)\left[s^{(j)}(\pm\theta_{\mathrm{w}}+h(z))-s^{(j)}(\pm\theta_{\mathrm{w}}-h(z))\right]\Big]\mathrm{d}z=0.\end{aligned} \tag{3.17}$$

[1] Note that in the alternative case where $\delta>2$, $z^je^{\pm i\delta z}$ would be replaced with $e^{\pm 2iz}$. This will also be true for (3.22).

Downloaded from https://academic.oup.com/imamat/article/85/3/421/5822762 by University of Cambridge user on 21 September 2020

We can now apply Malyuzhinets' theorem (see section 3.4 of Babich *et al.*, 2007 for details) to nullify the integral and produce the following set of functional equations:

$$q^{(j)}(\mp\bar{\theta}_{\mathrm{w}}+z)-q^{(j)}(\mp\bar{\theta}_{\mathrm{w}}-z)=h'(z)\left[s^{(j)}(\pm\theta_{\mathrm{w}}+h(z))-s^{(j)}(\pm\theta_{\mathrm{w}}-h(z))\right]. \tag{3.18}$$

For the application of Malyuzhinets' theorem to be valid, we should consider the possibility of branch cuts in the spectral functions. At this stage, it is difficult to specify the exact location of these branch cuts. Hence we must assume momentarily that there exists a half-strip region where the integrands are analytic in z. Such an assumption can be verified *a posteriori*. Note that in the initial case, $j=0$, we can apply the antisymmetry property (3.8) to simplify (3.18),

$$q^{(0)}(\mp\bar{\theta}_{\mathrm{w}}+z)-q^{(0)}(\mp\bar{\theta}_{\mathrm{w}}-z)=2h'(z)s^{(0)}(\pm\theta_{\mathrm{w}}+h(z)). \tag{3.19}$$

The second type of problem, $\mathcal{P}_{\Phi}^{(j)}$ where $j=1,2,3...$, is for the higher order components of the exterior solution $\Phi^{(j)}$, which are defined in Ω_1. These problems do not have any incoming plane waves either and satisfy inhomogeneous Neumann boundary conditions depending on the known $\Psi^{(j-1)}$ component.

$$\mathcal{P}_{\Phi}^{(j)}:\begin{cases}\nabla^2\Phi^{(j)}+k_1^2\Phi^{(j)}=0 & \text{(Governing equation)} \quad (3.20a)\\ \left.\dfrac{\partial\Phi^{(j)}}{\partial\theta}\right|_{\theta=\pm\theta_{\mathrm{w}}}=\left.\dfrac{\partial\Psi^{(j-1)}}{\partial\theta}\right|_{\theta=\pi\mp\bar{\theta}_{\mathrm{w}}} & \text{(Boundary conditions)} \quad (3.20b)\\ \text{Not applicable here} & \text{(Plane wave forcing)} \quad (3.20c)\\ \lim\limits_{r\to\infty}\displaystyle\int_{-\theta_{\mathrm{w}}}^{\theta_{\mathrm{w}}}\left|\frac{\partial\Phi_{\mathrm{Diff}}^{(j)}}{\partial r}-ik_1\Phi_{\mathrm{Diff}}^{(j)}\right|^2 r\mathrm{d}\theta=0 & \text{(Radiation condition)} \quad (3.20d)\\ \Phi^{(j)}=\mathcal{A}^{(j)}+O\left(r^{\delta}(\ln(r))^j\right) & \text{(Edge condition).} \quad (3.20e)\end{cases}$$

We seek a solution satisfying (3.20a) and (3.20d) in the form of (2.16),

$$\Phi^{(j)}=\frac{1}{2\pi i}\int_{\gamma_+}e^{-ik_1r\cos(z)}\left[s^{(j)}(\theta+z)-s^{(j)}(\theta-z)\right]\mathrm{d}z, \tag{3.21}$$

where, due to (3.20e), $s^{(j)}(z)$ has the following leading order behaviour as $\mathrm{Im}\{z\}\to\pm\infty$:

$$s^{(j)}(z)=\pm A^{(j)}+O\left(z^je^{\pm i\delta z}\right). \tag{3.22}$$

Downloaded from https://academic.oup.com/imamat/article/85/3/421/5822762 by University of Cambridge user on 21 September 2020

Note that for all j, $A^{(j)}$ in (3.22) is the same as $A^{(j)}$ in (3.14). No incoming plane waves means that $s^{(j)}(z)$ has no poles in the strip,

$$\left\{z : -\theta_{\mathrm{w}} < \mathrm{Re}\,\{z\} < \theta_{\mathrm{w}}\right\}. \tag{3.23}$$

Applying the boundary conditions, (3.20b), leads to the following:

$$\begin{aligned}\int_{\gamma_+} e^{-ik_1 r\cos(z)}(k_1\sin(z))\left[s^{(j)}(\pm\theta_{\mathrm{w}}+z)+s^{(j)}(\pm\theta_{\mathrm{w}}-z)\right]\mathrm{d}z \\ = \int_{\gamma_+} e^{-ik_2 r\cos(z)}(k_2\sin(z))\left[q^{(j-1)}(\mp\bar{\theta}_{\mathrm{w}}+z)+q^{(j-1)}(\mp\bar{\theta}_{\mathrm{w}}-z)\right]\mathrm{d}z.\end{aligned} \tag{3.24}$$

Here we apply the mapping $g(z)$, to transform the right hand side of (3.24), deform the mapped Sommerfeld contour back to the original and apply Malyuzhinets' theorem to produce the following set of functional equations:

$$s^{(j)}(\pm\theta_{\mathrm{w}}+z)+s^{(j)}(\pm\theta_{\mathrm{w}}-z) = q^{(j-1)}(\mp\bar{\theta}_{\mathrm{w}}+g(z))+q^{(j-1)}(\mp\bar{\theta}_{\mathrm{w}}-g(z)). \tag{3.25}$$

The two types of unsolved problems stated above will be called inhomogeneous Dirichlet ($\mathcal{P}_{\Psi}^{(j)}$) and inhomogeneous Neumann ($\mathcal{P}_{\Phi}^{(j)}$). In the next section, we shall combine elements from the papers Shanin (1998), Daniele (2003b) and Nethercote *et al.* (2020) (that use the Wiener–Hopf technique for impenetrable wedge problems) to find the unknown spectral functions $q^{(j)}(z)$ and $s^{(j)}(z)$.

4. Formulation and solution of the Wiener–Hopf problems

The basis of this method is to Laplace transform the total field, Φ or Ψ, and their θ derivative on the two wedge faces, $\theta = \pm\theta_{\mathrm{w}}$, and the line of symmetry $\theta = 0$ or π. By applying Green's second identity, these transforms are used to produce the Wiener–Hopf equations. After the boundary conditions are considered, a mapping to a new complex plane is introduced so that the Wiener–Hopf technique can be applied to produce a solution. Much of this procedure is discussed in section 3 of Nethercote *et al.* (2020).

Following the same method as section 3.2 in Nethercote *et al.* (2020), we solve these wedge problems by deriving two Wiener–Hopf equations. Let u represent one of the total fields ($\Phi^{(j)}$ or $\Psi^{(j)}$) and use the following definition of the Laplace transform (and associated inverse):

$$F(\eta) = \int_0^{\infty} f(r)e^{ikr\eta}\mathrm{d}r, \quad f(r) = \frac{k}{2\pi}\int_{-\infty}^{\infty} F(\eta)e^{-ikr\eta}\mathrm{d}\eta, \tag{4.1}$$

where $F(\eta)$ is analytic in the upper half-plane $\mathrm{Im}\,\{\eta\} > 0$ provided that $f(r)$ grows no faster than a power of r as $r \to \infty$. Hence we can define the following transforms of u and its θ derivative:

$$U(\eta,\theta) = \int_0^{\infty} u(r,\theta)e^{ikr\eta}\mathrm{d}r, \quad V(\eta,\theta) = \int_0^{\infty} \frac{1}{ikr}\frac{\partial u}{\partial\theta}(r,\theta)e^{ikr\eta}\mathrm{d}r. \tag{4.2}$$

Downloaded from https://academic.oup.com/imamat/article/85/3/421/5822762 by University of Cambridge user on 21 September 2020

This is done for two wedge regions $\theta \in [0, \Theta]$ and $\theta \in [-\Theta, 0]$, where $\Theta = \theta_w$ or $\bar{\theta}_w$ and results in the two Wiener–Hopf equations,

$$\begin{aligned} 2V(\cos(z),0) &= V(\cos(\Theta - z), -\Theta) + V(\cos(\Theta - z), \Theta) \\ &\quad - \sin(\Theta - z)\left[U(\cos(\Theta - z), -\Theta) - U(\cos(\Theta - z), \Theta)\right], \\ 2\sin(z)U(\cos(z),0) &= V(\cos(\Theta - z), -\Theta) - V(\cos(\Theta - z), \Theta) \\ &\quad - \sin(\Theta - z)\left[U(\cos(\Theta - z), -\Theta) + U(\cos(\Theta - z), \Theta)\right]. \end{aligned} \tag{4.3}$$

We solve the system (4.3) for $U(\cos(z),0)$ and $V(\cos(z),0)$ in terms of the known boundary data $V(\cos(\Theta - z), \pm\Theta)$ or $U(\cos(\Theta - z), \pm\Theta)$. From section 3.2 of Nethercote *et al.* (2020), it can be shown that if u is written as a Sommerfeld integral,

$$u(r,\theta) = \frac{1}{2\pi i}\int_{\gamma_+} e^{-ikr\cos(z)}\left[p(\theta + z) - p(\theta - z)\right] \mathrm{d}z, \tag{4.4}$$

then the Laplace transforms U and V can be written in terms of the spectral function $p(z)$,

$$U(\cos(z),\theta) = \frac{p(\theta + z) - p(\theta - z)}{ik\sin(z)}, \tag{4.5}$$

$$V(\cos(z),\theta) = \frac{i}{k}\left[p(\theta + z) + p(\theta - z)\right], \tag{4.6}$$

to show that,

$$p(z) = \frac{k}{2i}\left[V(\cos(z),0) - \sin(z)U(\cos(z),0)\right]. \tag{4.7}$$

For the initial homogeneous Neumann problem, we will have $u = \Phi^{(0)}$, $p = s^{(0)}$, $k = k_1$, $\Theta = \theta_w$ and the boundary conditions, $V(\cos(\Theta - z), \pm\theta_w) = 0$. In this case, we needed to factorize $\sin(z)$ and remove the poles on the right-hand side of (4.3) to ensure that the two sides have a common domain of analyticity. With the boundedness of the terms, we used Liouville's theorem to determine both $U(\cos(z),0)$ and $V(\cos(z),0)$ and hence show (3.7) (see section 3 of Nethercote *et al.*, 2020 for further details).

For the other problems, we will have inhomogeneous Neumann/Dirichlet boundary conditions and we will also need to alternate between wavenumbers $k = k_1, k_2$ and the wedge angle $\Theta = \theta_w, \bar{\theta}_w$. Fortunately, there are no plane wave sources that need removing this time.

4.1 *Inhomogeneous Dirichlet problem* $\left(\mathcal{P}_\Psi^{(j)}\right)$

In these problems, the total wave field $\Psi^{(j)}$ is in the interior of the wedge (Ω_2) hence we have $k = k_2$ and $\Theta = \bar{\theta}_w$. To make this a little simpler, put Green's second identity in the $(r, \widehat{\theta})$ coordinate system

Downloaded from https://academic.oup.com/imamat/article/85/3/421/5822762 by University of Cambridge user on 21 September 2020

where $\widehat{\theta} = \theta - \pi$. Hence we have $u(r, \widehat{\theta}) = \Psi^{(j)}(r, \pi + \widehat{\theta})$ (with $j = 0, 1, 2...$). Define the known boundary data as U_1 and U_2 using the following definitions:[2]

$$U_1(z) = U(\cos(\bar{\theta}_\mathrm{w} - z), \bar{\theta}_\mathrm{w}) = \int_0^\infty \Psi^{(j)}(r, \pi + \bar{\theta}_\mathrm{w}) e^{ik_2 r \cos(\bar{\theta}_\mathrm{w} - z)} \mathrm{d}r, \tag{4.8}$$

$$U_2(z) = U(\cos(\bar{\theta}_\mathrm{w} - z), -\bar{\theta}_\mathrm{w}) = \int_0^\infty \Psi^{(j)}(r, \pi - \bar{\theta}_\mathrm{w}) e^{ik_2 r \cos(\bar{\theta}_\mathrm{w} - z)} \mathrm{d}r. \tag{4.9}$$

Both of these definitions can be expressed explicitly in terms of $s^{(j)}$ using the identity (4.5) and the boundary functional conditions (3.18),

$$U_1(z) = \frac{h'(\bar{\theta}_\mathrm{w} - z)}{ik_2 \sin(\bar{\theta}_\mathrm{w} - z)} \left[s^{(j)}(-\theta_\mathrm{w} + h(\bar{\theta}_\mathrm{w} - z)) - s^{(j)}(-\theta_\mathrm{w} - h(\bar{\theta}_\mathrm{w} - z)) \right], \tag{4.10}$$

$$U_2(z) = \frac{h'(\bar{\theta}_\mathrm{w} - z)}{ik_2 \sin(\bar{\theta}_\mathrm{w} - z)} \left[s^{(j)}(\theta_\mathrm{w} + h(\bar{\theta}_\mathrm{w} - z)) - s^{(j)}(\theta_\mathrm{w} - h(\bar{\theta}_\mathrm{w} - z)) \right]. \tag{4.11}$$

The Wiener–Hopf system (4.3) becomes,

$$\begin{aligned} V(\cos(z), 0) =& \frac{1}{2} \left[V(\cos(\bar{\theta}_\mathrm{w} - z), -\bar{\theta}_\mathrm{w}) + V(\cos(\bar{\theta}_\mathrm{w} - z), \bar{\theta}_\mathrm{w}) \right] + \frac{1}{2} \sin(\bar{\theta}_\mathrm{w} - z) \left[U_1(z) - U_2(z) \right], \\ \sin(z) U(\cos(z), 0) =& \frac{1}{2} \left[V(\cos(\bar{\theta}_\mathrm{w} - z), -\bar{\theta}_\mathrm{w}) - V(\cos(\bar{\theta}_\mathrm{w} - z), \bar{\theta}_\mathrm{w}) \right] - \frac{1}{2} \sin(\bar{\theta}_\mathrm{w} - z) \left[U_1(z) + U_2(z) \right]. \end{aligned} \tag{4.12}$$

In this form, the Wiener–Hopf technique fails because this system cannot be factorized. To counter this issue, we will need to map these equations onto a new complex plane so that they can be reduced to classical Wiener–Hopf equations similar to those in Noble (1958). We will conformally map z so that $U(\cos(z), 0)$ and $V(\cos(z), 0)$ are analytic on an upper half plane and $V(\cos(\bar{\theta}_\mathrm{w} - z), \pm\bar{\theta}_\mathrm{w})$ are analytic on a lower half plane. This is achieved using the following mapping with $\Theta = \bar{\theta}_\mathrm{w}$:

$$z(\alpha) = \frac{\Theta}{\pi} \cos^{-1}(\alpha), \quad \alpha(z) = \cos\left(\frac{\pi}{\Theta} z\right). \tag{4.13}$$

Equation (4.13) has a single branch cut along the real line segment $\alpha \in (-\infty, -1]$ where the local argument of the chosen branch is $(-\pi, \pi]$. This is done by choosing the branch of the inverse cosine such that $\Theta - z(\alpha) = z(-\alpha)$. Note that this mapping limits z to belong to the strip $\mathrm{Re}\{z\} \in [0, \Theta]$. For further details, see section 3.1 of Nethercote *et al.* (2020) and references within such as, Shanin (1996) and Daniele (2003b).

[2] In this subsection and the next, we do not state the j dependency for the functions U, V, U_1, U_2, V_1 and V_2 for ease of notation.

Downloaded from https://academic.oup.com/imamat/article/85/3/421/5822762 by University of Cambridge user on 21 September 2020

Now we apply (4.13) to the Wiener–Hopf system (4.12) to transform it onto the α-plane,

$$V(\cos(z(\alpha)),0) = \frac{1}{2}\left[V(\cos(z(-\alpha)),-\bar{\theta}_{\mathrm{w}}) + V(\cos(z(-\alpha)),\bar{\theta}_{\mathrm{w}})\right] + \frac{1}{2}\sin(z(-\alpha))\left[U_1(z(\alpha)) - U_2(z(\alpha))\right], \tag{4.14}$$

$$\sin(z(\alpha))U(\cos(z(\alpha)),0) = \frac{1}{2}\left[V(\cos(z(-\alpha)),-\bar{\theta}_{\mathrm{w}}) - V(\cos(z(-\alpha)),\bar{\theta}_{\mathrm{w}})\right] - \frac{1}{2}\sin(z(-\alpha))\left[U_1(z(\alpha)) + U_2(z(\alpha))\right]. \tag{4.15}$$

To proceed with the Wiener–Hopf method, we will require to factorize $\sin(z(\alpha))$ in equation (4.15). Before performing this factorization, we shall define the domains $\mathcal{R}_{\pm}$ on which this factorization will be done:

$$\mathcal{R}_+ = \{\alpha : \mathrm{Im}\{\alpha\} > 0\} \cup \{\alpha : \mathrm{Re}\{\alpha\} > -1, \mathrm{Im}\{\alpha\} = 0\} \tag{4.16}$$

$$\mathcal{R}_- = \{\alpha : \mathrm{Im}\{\alpha\} < 0\} \cup \{\alpha : \mathrm{Re}\{\alpha\} < 1, \mathrm{Im}\{\alpha\} = 0\}. \tag{4.17}$$

Note that $\mathcal{R}_+ \cup \mathcal{R}_-$ is the whole complex plane and $\mathcal{R}_+ \cap \mathcal{R}_-$ is the real line segment $\alpha \in (-1,1)$. We expect $V(\cos(z(\alpha)),0)$ and $U(\cos(z(\alpha)),0)$ to be analytic on $\mathcal{R}_+$ and have a branch cut on the real line segment $\alpha \in (-\infty,-1]$. We also expect $V(\cos(z(-\alpha)),\pm\bar{\theta}_{\mathrm{w}})$ to be analytic on $\mathcal{R}_-$ and have a branch cut on the real line segment $\alpha \in [1,\infty)$. However, $\sin(z(\alpha))$ has both branch cuts, which is why it must be factorized. To factorize $\sin(z(\alpha))$, we refer to section 3.1 of Nethercote *et al.* (2020), where it was found that,

$$\sin(z(\alpha)) = f_-(\alpha) \times f_+(\alpha) = \frac{\sqrt{2-2\alpha}}{2} \times \left(\frac{\sin\left(\frac{\bar{\theta}_{\mathrm{w}}}{\pi}\cos^{-1}(\alpha)\right)}{\frac{\sqrt{2-2\alpha}}{2}}\right). \tag{4.18}$$

This means that (4.15) after factorization becomes,

$$f_+(\alpha)U(\cos(z(\alpha)),0) = \frac{1}{2f_-(\alpha)}\left[V(\cos(z(-\alpha)),-\bar{\theta}_{\mathrm{w}}) - V(\cos(z(-\alpha)),\bar{\theta}_{\mathrm{w}})\right] - \frac{\sin(z(-\alpha))}{2f_-(\alpha)}\left[U_1(z(\alpha)) + U_2(z(\alpha))\right]. \tag{4.19}$$

The first terms in (4.14) and (4.19) are analytic at $\alpha = 1$, hence are analytic on the upper half α-plane $\mathcal{R}_+$. The second terms are analytic at $\alpha = -1$, hence are analytic on the lower half α-plane $\mathcal{R}_-$.

Downloaded from https://academic.oup.com/imamat/article/85/3/421/5822762 by University of Cambridge user on 21 September 2020

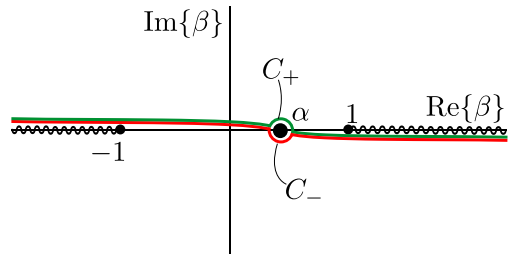

FIG. 5. Diagram of the contours C_- (in red) and C_+ (in green) in the β-plane. Here there is a pole at $\beta = \alpha$ and branch points at $\beta = \pm 1$.

The last terms in both equations are only analytic on the real line segment $\alpha \in \mathcal{R}_+ \cap \mathcal{R}_-$. We define $M_1(\alpha)$ and $M_2(\alpha)$ as,

$$M_1(\alpha) = \frac{1}{2}\sin(z(-\alpha))\left[U_1(z(\alpha)) - U_2(z(\alpha))\right],$$
$$M_2(\alpha) = \frac{\sin(z(-\alpha))}{2f_-(\alpha)}\left[U_1(z(\alpha)) + U_2(z(\alpha))\right]. \tag{4.20}$$

We use Cauchy's integral formula to sum split (4.20) into two terms analytic in $\mathcal{R}_+$ and $\mathcal{R}_-$, respectively. For $n = 1, 2$, we use the following sum split, $M_n(\alpha) = M_{n+}(\alpha) + M_{n-}(\alpha)$,

$$\text{where, } M_{n+}(\alpha) = \frac{1}{2\pi i}\int_{C_-}\frac{M_n(\beta)}{\beta-\alpha}\mathrm{d}\beta, \quad M_{n-}(\alpha) = -\frac{1}{2\pi i}\int_{C_+}\frac{M_n(\beta)}{\beta-\alpha}\mathrm{d}\beta. \tag{4.21}$$

Using these formulae, $M_{n+}(\alpha)$ (resp. $M_{n-}(\alpha)$) can be analytically continued onto the half-plane $\mathcal{R}_+$ (resp. $\mathcal{R}_-$).

The contour C_- runs from $-\infty + i0$ to $\infty - i0$ underneath the simple pole at $\beta = \alpha$. The contour C_+ runs between $-\infty + i0$ to $\infty - i0$ above C_- and above the simple pole at $\beta = \alpha$. Both these contours are illustrated on Fig. 5 in red and green, respectively. We create the following entire functions from the Wiener–Hopf equations.

$$\mathcal{M}_1(\alpha) = \begin{cases} V(\cos(z(\alpha)),0) - M_{1+}(\alpha) & \alpha \in \mathcal{R}_+, \\ \frac{1}{2}\left[V(\cos(z(-\alpha)),-\bar{\theta}_{\mathrm{w}}) + V(\cos(z(-\alpha)),\bar{\theta}_{\mathrm{w}})\right] + M_{1-}(\alpha) & \alpha \in \mathcal{R}_-, \\ (4.14) & \alpha \in \mathcal{R}_+ \cap \mathcal{R}_-, \end{cases}$$

$$\mathcal{M}_2(\alpha) = \begin{cases} \frac{2\sin(z(\alpha))}{\sqrt{2-2\alpha}}U(\cos(z(\alpha)),0) + M_{2+}(\alpha) & \alpha \in \mathcal{R}_+, \\ \frac{1}{\sqrt{2-2\alpha}}\left[V(\cos(z(-\alpha)),-\bar{\theta}_{\mathrm{w}}) - V(\cos(z(-\alpha)),\bar{\theta}_{\mathrm{w}})\right] - M_{2-}(\alpha) & \alpha \in \mathcal{R}_-, \\ (4.19) & \alpha \in \mathcal{R}_+ \cap \mathcal{R}_-. \end{cases}$$

Noting that due to the edge conditions, we can show that each of these terms tends to zero as $|\alpha| \to \infty$. This means that we can apply Liouville's theorem to get,

$$V(\cos(z),0) = M_{1+}(\alpha(z)), \tag{4.22}$$

$$\sin(z)U(\cos(z),0) = -\sin\left(\bar{\delta}z\right)M_{2+}(\alpha(z)), \tag{4.23}$$

Downloaded from https://academic.oup.com/imamat/article/85/3/421/5822762 by University of Cambridge user on 21 September 2020

where we have used $f_-(\alpha(z)) = \sin(\bar{\delta}z)$ with $\bar{\delta} = \pi/(2\bar{\theta}_\mathrm{w})$. We write $q^{(j)}(z)$ in terms of these Cauchy integrals,

$$\begin{aligned} q^{(j)}(z) &= \frac{k_2}{2i}\left[V(\cos(z),0) - \sin(z)U(\cos(z),0)\right], \\ &= \frac{k_2}{2i}\left[M_{1+}(\alpha(z)) + \sin\left(\bar{\delta}z\right)M_{2+}(\alpha(z))\right], \\ &= \frac{1}{2\pi i}\int_{C_-} \frac{k_2(M_1(\beta) + \sin\left(\bar{\delta}z\right)M_2(\beta))}{2i(\beta - \alpha(z))}\mathrm{d}\beta. \end{aligned} \tag{4.24}$$

We substitute the definitions (4.20) for M_1 and M_2 and use (4.13) to obtain

$$\begin{aligned} q^{(j)}(z) = \frac{1}{2\pi i}\int_{C_-} \frac{k_2 \sin\left(\bar{\theta}_\mathrm{w} - \zeta(\beta)\right)}{2i(\beta - \alpha(z))\sqrt{2-2\beta}}\Bigg[\left(\sqrt{\frac{1-\beta}{2}} + \sin\left(\bar{\delta}z\right)\right)U_1(\zeta(\beta)) \\ - \left(\sqrt{\frac{1-\beta}{2}} - \sin\left(\bar{\delta}z\right)\right)U_2(\zeta(\beta))\Bigg]\mathrm{d}\beta, \end{aligned} \tag{4.25}$$

where $\zeta(\beta) = \frac{\bar{\theta}_\mathrm{w}}{\pi}\cos^{-1}(\beta)$. We want to transform (4.25) to the ζ-plane. Noting that,

$$\beta = \cos\left(2\bar{\delta}\zeta\right), \quad \sqrt{\frac{1-\beta}{2}} = \sin\left(\bar{\delta}\zeta\right) \text{ and } \frac{\mathrm{d}\beta}{\mathrm{d}\zeta} = -2\bar{\delta}\sin\left(2\bar{\delta}\zeta\right), \tag{4.26}$$

(4.25) becomes,

$$\begin{aligned} q^{(j)}(z) = \frac{1}{4\pi i}\int_C \Bigg(\frac{\bar{\delta}\cos\left(\bar{\delta}\zeta\right)}{\sin\left(\bar{\delta}\zeta\right) + \sin\left(\bar{\delta}z\right)}\left(ik_2\sin\left(\bar{\theta}_\mathrm{w} - \zeta\right)U_2(\zeta)\right) \\ - \frac{\bar{\delta}\cos\left(\bar{\delta}\zeta\right)}{\sin\left(\bar{\delta}\zeta\right) - \sin\left(\bar{\delta}z\right)}\left(ik_2\sin\left(\bar{\theta}_\mathrm{w} - \zeta\right)U_1(\zeta)\right)\Bigg)\mathrm{d}\zeta. \end{aligned} \tag{4.27}$$

The original contour C_- is transformed to C (shown on Fig. 6 in red where $\Theta = \bar{\theta}_\mathrm{w}$) that runs from $\zeta = \bar{\theta}_\mathrm{w} - i\infty$ to $i\infty$ via the points $\bar{\theta}_\mathrm{w}$, 0 and above the pole at $\zeta = z$. We deform the contour to the straight line running from $\zeta = \bar{\theta}_\mathrm{w} - i\infty$ to $\bar{\theta}_\mathrm{w} + i\infty$ (shown on Fig. 6 in blue).

This deformation does not cross any singularities so,

$$\begin{aligned} q^{(j)}(z) = \frac{1}{4\pi i}\int_{\bar{\theta}_\mathrm{w}-i\infty}^{\bar{\theta}_\mathrm{w}+i\infty} \Bigg(\frac{\bar{\delta}\cos\left(\bar{\delta}\zeta\right)}{\sin\left(\bar{\delta}\zeta\right) + \sin\left(\bar{\delta}z\right)}\left(ik_2\sin\left(\bar{\theta}_\mathrm{w} - \zeta\right)U_2(\zeta)\right) \\ - \frac{\bar{\delta}\cos\left(\bar{\delta}\zeta\right)}{\sin\left(\bar{\delta}\zeta\right) - \sin\left(\bar{\delta}z\right)}\left(ik_2\sin\left(\bar{\theta}_\mathrm{w} - \zeta\right)U_1(\zeta)\right)\Bigg)\mathrm{d}\zeta. \end{aligned} \tag{4.28}$$

Downloaded from https://academic.oup.com/imamat/article/85/3/421/5822762 by University of Cambridge user on 21 September 2020

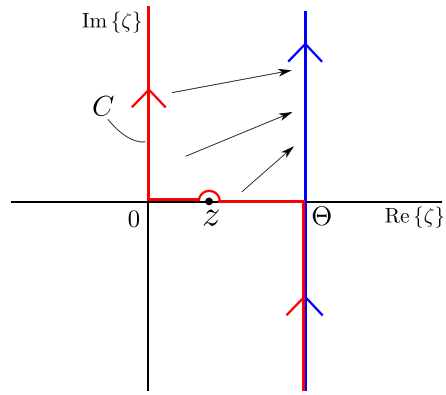

FIG. 6. Diagram of the contour C_- before and after deformation (in red and blue, respectively) in the ζ-plane.

We substitute the two definitions for $U_1(\zeta)$ and $U_2(\zeta)$, (4.10) and (4.11), to put the integrands in terms of $s^{(j)}$

$$q^{(j)}(z) = \frac{1}{4\pi i}\int_{\bar\theta_w - i\infty}^{\bar\theta_w + i\infty} \left(\frac{\bar\delta\cos\left(\bar\delta\zeta\right)h'(\bar\theta_w - \zeta)}{\sin\left(\bar\delta\zeta\right)+\sin\left(\bar\delta z\right)}\left[s^{(j)}(\theta_w + h(\bar\theta_w - \zeta)) - s^{(j)}(\theta_w - h(\bar\theta_w - \zeta))\right] \right.$$
$$\left. - \frac{\bar\delta\cos\left(\bar\delta\zeta\right)h'(\bar\theta_w - \zeta)}{\sin\left(\bar\delta\zeta\right)-\sin\left(\bar\delta z\right)}\left[s^{(j)}(-\theta_w + h(\bar\theta_w - \zeta)) - s^{(j)}(-\theta_w - h(\bar\theta_w - \zeta))\right]\right)\mathrm{d}\zeta. \tag{4.29}$$

This integrand can be simplified further with the substitution, $\zeta \mapsto \bar\theta_w - \zeta$ to obtain the final formula,

$$q^{(j)}(z) = \frac{1}{4\pi i}\int_{-i\infty}^{i\infty} \left(\frac{\bar\delta\sin\left(\bar\delta\zeta\right)h'(\zeta)}{\cos\left(\bar\delta\zeta\right)+\sin\left(\bar\delta z\right)}\left[s^{(j)}(\theta_w + h(\zeta)) - s^{(j)}(\theta_w - h(\zeta))\right] \right.$$
$$\left. - \frac{\bar\delta\sin\left(\bar\delta\zeta\right)h'(\zeta)}{\cos\left(\bar\delta\zeta\right)-\sin\left(\bar\delta z\right)}\left[s^{(j)}(-\theta_w + h(\zeta)) - s^{(j)}(-\theta_w - h(\zeta))\right]\right)\mathrm{d}\zeta. \tag{4.30}$$

Evaluation of this integral formula is difficult due to the numerous singularities of the integrand. The functions $h(\zeta)$ and $h'(\zeta)$ indicate the presence of an infinite number of branch cuts; however, their combination causes the cut centred at the origin to be cancelled out. The spectral functions $s^{(j)}$ have an infinite number of simple poles, which we will call the spectral poles, located either on the real line or the branch cuts. The rest of the integrand contributes one last set of simple poles located at $\zeta = (2n-1)\bar\theta_w \pm z$ where $n \in \mathbb{Z}$, which we will call the z-poles.

This integral formula for $q^{(j)}(z)$ is valid for $|\mathrm{Re}\{z\}| < \bar\theta_w$; however, when z is outside this strip, the contour must deform so that it passes in between the pair of poles at $\zeta = \pm\bar\theta_w - z$ and also in between the pair of poles at $\zeta = \pm\bar\theta_w + z$. This is demonstrated in Fig. 7 with $\Theta = \bar\theta_w$.

Using the ideas from Fig. 7, it is not difficult to show that the formula (4.30) satisfies the boundary functional conditions (3.18). For the initial inhomogeneous Dirichlet problem (for $j = 0$), the formula

Downloaded from https://academic.oup.com/imamat/article/85/3/421/5822762 by University of Cambridge user on 21 September 2020

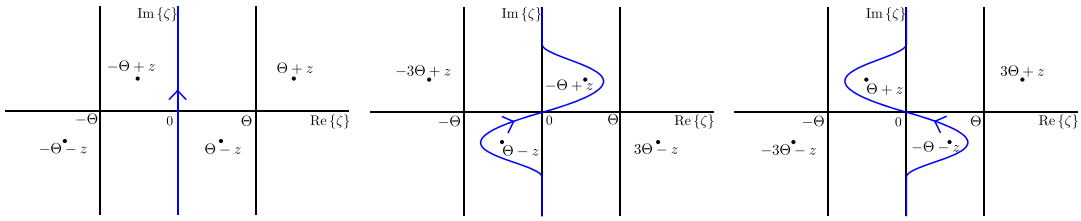

FIG. 7. The local pole locations and the normal integration contour for $|\mathrm{Re}\,\{z\}| < \Theta$ (left). The local pole locations and the adapted integration contour for $\mathrm{Re}\,\{z\} > \Theta$ (middle). The local pole locations and the adapted integration contour for $\mathrm{Re}\,\{z\} < -\Theta$ (right). Note that if $\mathrm{Im}\,\{z\} < 0$ then all these images are flipped vertically.

(4.30) simplifies further using the antisymmetry property (3.8),

$$q^{(0)}(z) = \frac{1}{2\pi i}\int_{-i\infty}^{i\infty}\left(\frac{\bar{\delta}\sin\left(\bar{\delta}\zeta\right)h'(\zeta)s^{(0)}(\theta_{\mathrm{w}}+h(\zeta))}{\cos\left(\bar{\delta}\zeta\right)+\sin\left(\bar{\delta}z\right)} - \frac{\bar{\delta}\sin\left(\bar{\delta}\zeta\right)h'(\zeta)s^{(0)}(-\theta_{\mathrm{w}}+h(\zeta))}{\cos\left(\bar{\delta}\zeta\right)-\sin\left(\bar{\delta}z\right)}\right)\mathrm{d}\zeta. \quad (4.31)$$

We discuss the asymptotic behaviour of (4.31) as $\mathrm{Im}\,\{z\} \to \pm\infty$ in Appendix B. We should also note that if $s^{(j)}(z^*) = \left(s^{(j)}(z)\right)^*$, then $q^{(j)}(z^*) = \left(q^{(j)}(z)\right)^*$, which can be shown using (4.30) for all j.

4.2 *Inhomogeneous Neumann problem* $\left(\mathcal{P}_{\Phi}^{(j+1)}\right)$

For these problems, the total wave field $\Phi^{(j+1)}$ is exterior to the wedge scatterer hence we have $k = k_1$, $\Theta = \theta_{\mathrm{w}}$, $u(r,\theta) = \Phi^{(j+1)}(r,\theta)$ (with $j = 0, 1, 2...$). We define the known boundary data as V_1 and V_2 with the following definitions:

$$V_1(z) = V(\cos(\theta_{\mathrm{w}}-z),\theta_{\mathrm{w}}) = \int_0^\infty \frac{1}{ik_1 r}\frac{\partial\Phi^{(j+1)}}{\partial\theta}\bigg|_{\theta=\theta_{\mathrm{w}}} e^{ik_1 r\cos(\theta_{\mathrm{w}}-z)}\mathrm{d}r, \quad (4.32)$$

$$V_2(z) = V(\cos(\theta_{\mathrm{w}}-z),-\theta_{\mathrm{w}}) = \int_0^\infty \frac{1}{ik_1 r}\frac{\partial\Phi^{(j+1)}}{\partial\theta}\bigg|_{\theta=-\theta_{\mathrm{w}}} e^{ik_1 r\cos(\theta_{\mathrm{w}}-z)}\mathrm{d}r. \quad (4.33)$$

Both of these definitions can be expressed explicitly in terms of $q^{(j)}$ using the identity (4.6) and the boundary functional conditions (3.25), leading to

$$V_1(z) = \frac{i}{k_1}\left[q^{(j)}(-\bar{\theta}_{\mathrm{w}}+g(\theta_{\mathrm{w}}-z)) + q^{(j)}(-\bar{\theta}_{\mathrm{w}}-g(\theta_{\mathrm{w}}-z))\right], \quad (4.34)$$

$$V_2(z) = \frac{i}{k_1}\left[q^{(j)}(\bar{\theta}_{\mathrm{w}}+g(\theta_{\mathrm{w}}-z)) + q^{(j)}(\bar{\theta}_{\mathrm{w}}-g(\theta_{\mathrm{w}}-z))\right]. \quad (4.35)$$

Downloaded from https://academic.oup.com/imamat/article/85/3/421/5822762 by University of Cambridge user on 21 September 2020

The Wiener–Hopf system (4.3) is therefore,

$$\begin{aligned} V(\cos(z),0) &= -\frac{1}{2}\sin(\theta_{\mathrm{w}}-z)\left[U(\cos(\theta_{\mathrm{w}}-z),-\theta_{\mathrm{w}})-U(\cos(\theta_{\mathrm{w}}-z),\theta_{\mathrm{w}})\right]+\frac{1}{2}\left[V_1(z)+V_2(z)\right], \\ \sin(z)U(\cos(z),0) &= -\frac{1}{2}\sin(\theta_{\mathrm{w}}-z)\left[U(\cos(\theta_{\mathrm{w}}-z),-\theta_{\mathrm{w}})+U(\cos(\theta_{\mathrm{w}}-z),\theta_{\mathrm{w}})\right]-\frac{1}{2}\left[V_1(z)-V_2(z)\right]. \end{aligned} \tag{4.36}$$

The method to solve the Wiener–Hopf system (4.36) is the same as the inhomogeneous Dirichlet problems except for a few key differences. This time we will need to reuse the mapping (4.13) with $\Theta = \theta_{\mathrm{w}}$ and we will also need to factorize both $\sin(z)$ and $\sin(\theta_{\mathrm{w}}-z)$ (see section 3.1 in Nethercote *et al.*, 2020). The end result is the following integral formula:

$$\begin{aligned} s^{(j+1)}(z) = \frac{1}{4\pi i}\int_{-i\infty}^{i\infty}\Bigg(&\frac{\delta\cos(\delta z)}{\cos(\delta\zeta)+\sin(\delta z)}\left[q^{(j)}(\bar{\theta}_{\mathrm{w}}+g(\zeta))+q^{(j)}(\bar{\theta}_{\mathrm{w}}-g(\zeta))\right] \\ &+\frac{\delta\cos(\delta z)}{\cos(\delta\zeta)-\sin(\delta z)}\left[q^{(j)}(-\bar{\theta}_{\mathrm{w}}+g(\zeta))+q^{(j)}(-\bar{\theta}_{\mathrm{w}}-g(\zeta))\right]\Bigg)\mathrm{d}\zeta. \end{aligned} \tag{4.37}$$

The evaluation of this formula has shared difficulties with (4.30). The presence of $g(\zeta)$ will produce an infinite number of branch cuts, but the cut centred at the origin is cancelled out. The $q^{(j)}$ functions have an infinite number of simple poles contained on the real line (called the spectral poles). The rest of the integrand contributes one last set of simple poles located at $\zeta = (2n-1)\theta_{\mathrm{w}} \pm z$ where $n \in \mathbb{Z}$ (called the z-poles).

This integral formula for $s^{(j+1)}(z)$ is valid for $|\mathrm{Re}\{z\}| < \theta_{\mathrm{w}}$; however, when z is outside this strip the contour must deform so that it passes in between the pair of poles at $\zeta = \pm\theta_{\mathrm{w}} - z$ and also in between the pair of poles at $\zeta = \pm\theta_{\mathrm{w}} + z$. This is demonstrated in Fig. 7 with $\Theta = \theta_{\mathrm{w}}$.

Similarly to (4.30), it is not difficult to show that the formula (4.37) satisfies the boundary functional conditions (3.25). Also note that if $q^{(j)}(z^*) = (q^{(j)}(z))^*$ then $s^{(j+1)}(z^*) = (s^{(j+1)}(z))^*$, which alongside the last note of Section 4.1 and the conjugacy property (3.10) allows us to conclude that $q^{(j)}$ and $s^{(j)}$ satisfy the property $p(z^*) = (p(z))^*$ for all j.

Recall the alternate case in the edge conditions where $\delta > 2$. The above methodology does not change and the functions used in Liouville's theorem ($\mathcal{M}_1$ and $\mathcal{M}_2$) will still decay to zero as $|\alpha| \to \infty$ preserving the obtained solution in this case.

4.3 *Example: penetrable half-space*

As an example to test (4.30) and (4.37), we will look at a simple case where the exact solution can be derived using conventional methods. In this example, we set $\bar{\theta}_{\mathrm{w}} = \theta_{\mathrm{w}} = \frac{\pi}{2}$ (corresponding to a half-space problem) so that the scattered part of the solution consists of a single reflected wave and a single transmitted wave,

$$\Phi(r,\theta) = \Phi_{\mathrm{I}} + R\Phi_{\mathrm{R}}, \quad \Psi(r,\theta) = T\Phi_{\mathrm{T}}. \tag{4.38}$$

Downloaded from https://academic.oup.com/imamat/article/85/3/421/5822762 by University of Cambridge user on 21 September 2020

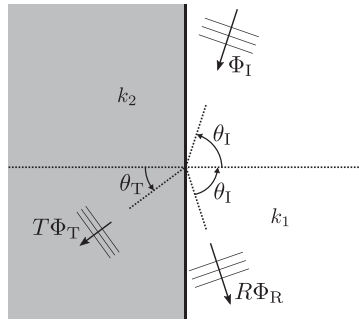

FIG. 8. Penetrable half-space geometry.

Here Φ_{I}, Φ_{R} and Φ_{T} represent the incident, reflected and transmitted waves respectively and are given by

$$\Phi_{\mathrm{I}} = e^{-ik_1 r\cos(\theta-\theta_{\mathrm{I}})}, \quad \Phi_{\mathrm{R}} = e^{ik_1 r\cos(\theta+\theta_{\mathrm{I}})}, \quad \Phi_{\mathrm{T}} = e^{-ik_2 r\cos(\theta-\theta_{\mathrm{T}})}. \tag{4.39}$$

The transmission angle θ_{T} is found using Snell's law,

$$\theta_{\mathrm{T}} = \sin^{-1}\left(\lambda_k \sin(\theta_{\mathrm{I}})\right) = \frac{\pi}{2} - g\left(\frac{\pi}{2} - \theta_{\mathrm{I}}\right). \tag{4.40}$$

The reflection and transmission coefficients (R and T respectively) are determined by the boundary conditions,

$$T = R + 1, \quad R = \frac{\frac{\lambda_k \cos(\theta_{\mathrm{I}})}{\cos(\theta_{\mathrm{T}})} - \lambda}{\frac{\lambda_k \cos(\theta_{\mathrm{I}})}{\cos(\theta_{\mathrm{T}})} + \lambda} = 1 - \frac{2\lambda}{g'\left(\frac{\pi}{2} - \theta_{\mathrm{I}}\right) + \lambda}. \tag{4.41}$$

Figure 8 is a diagram illustrating the half-space and the components of the exact solution (4.38).

Finding the Taylor series expansion about $\lambda = 0$ of the exact solution (4.38) allows us to determine the expected solution of (4.30) and (4.37). Noting the expansions of the reflection and transmission coefficients,

$$R = 1 + 2\sum_{j=1}^{\infty}\left(\frac{-\lambda}{g'\left(\frac{\pi}{2} - \theta_{\mathrm{I}}\right)}\right)^j, \quad T = 2\sum_{j=0}^{\infty}\left(\frac{-\lambda}{g'\left(\frac{\pi}{2} - \theta_{\mathrm{I}}\right)}\right)^j, \tag{4.42}$$

each of the components in the high-contrast approximation are given as,

$$\Phi^{(0)} = \Phi_{\mathrm{I}} + \Phi_{\mathrm{R}}, \quad \Phi^{(j)} = 2\left(\frac{-1}{g'\left(\frac{\pi}{2} - \theta_{\mathrm{I}}\right)}\right)^j \Phi_{\mathrm{R}}, \quad j = 1, 2...,$$

$$\Psi^{(j)} = 2\left(\frac{-1}{g'\left(\frac{\pi}{2} - \theta_{\mathrm{I}}\right)}\right)^j \Phi_{\mathrm{T}}, \quad j = 0, 1, 2.... \tag{4.43}$$

Downloaded from https://academic.oup.com/imamat/article/85/3/421/5822762 by University of Cambridge user on 21 September 2020

We already know the corresponding spectral function for $\Phi^{(0)}$,

$$s^{(0)}(z) = \frac{\cos(z)}{\sin(z) - \sin(\theta_{\mathrm{I}})}. \tag{4.44}$$

We use formulae adapted from (4.7) to derive what to expect for the other spectral functions. This means that for $s^{(j)}(z)$,

$$\begin{aligned} s^{(j)}(z) &= \frac{ik_1}{2}\int_0^\infty \left[\sin(z)\Phi^{(j)} - \frac{1}{ik_1 r}\frac{\partial \Phi}{\partial \theta}^{(j)}\right]_{\theta=0} e^{ik_1 r\cos(z)}\mathrm{d}r, \\ &= -\left(\frac{-1}{g'\left(\frac{\pi}{2}-\theta_{\mathrm{I}}\right)}\right)^j \frac{\sin(z)+\sin(\theta_{\mathrm{I}})}{\cos(z)+\cos(\theta_{\mathrm{I}})}. \end{aligned} \tag{4.45}$$

Other equivalent forms for $s^{(j)}(z)$ are,

$$s^{(j)}(z) = \left(\frac{-1}{g'\left(\frac{\pi}{2}-\theta_{\mathrm{I}}\right)}\right)^j \frac{\cos(z)-\cos(\theta_{\mathrm{I}})}{\sin(z)-\sin(\theta_{\mathrm{I}})} = -\left(\frac{-1}{g'\left(\frac{\pi}{2}-\theta_{\mathrm{I}}\right)}\right)^j \tan\left(\frac{z+\theta_{\mathrm{I}}}{2}\right). \tag{4.46}$$

Similarly for $q^{(j)}(z)$,

$$\begin{aligned} q^{(j)}(z) &= \frac{ik_2}{2}\int_0^\infty \left[\sin(z)\Psi^{(j)} - \frac{1}{ik_2 r}\frac{\partial \Psi}{\partial \theta}^{(j)}\right]_{\theta=\pi} e^{ik_2 r\cos(z)}\mathrm{d}r, \\ &= -\left(\frac{-1}{g'\left(\frac{\pi}{2}-\theta_{\mathrm{I}}\right)}\right)^j \frac{\sin(z)-\sin(\theta_{\mathrm{T}})}{\cos(z)+\cos(\theta_{\mathrm{T}})}, \end{aligned} \tag{4.47}$$

with the other equivalent forms,

$$q^{(j)}(z) = \left(\frac{-1}{g'\left(\frac{\pi}{2}-\theta_{\mathrm{I}}\right)}\right)^j \frac{\cos(z)-\cos(\theta_{\mathrm{T}})}{\sin(z)+\sin(\theta_{\mathrm{T}})} = -\left(\frac{-1}{g'\left(\frac{\pi}{2}-\theta_{\mathrm{I}}\right)}\right)^j \tan\left(\frac{z-\theta_{\mathrm{T}}}{2}\right). \tag{4.48}$$

We now rederive $q^{(j)}(z)$ and $s^{(j)}(z)$ via the integrals (4.30) and (4.37) as proof of validity in the half-space case. For $q^{(0)}(z)$, we use (4.31), noting that $\delta = \bar{\delta} = 1$,

$$q^{(0)}(z) = \frac{1}{2\pi i}\int_{-i\infty}^{i\infty}\left(\frac{\sin(\zeta)h'(\zeta)s^{(0)}\left(\frac{\pi}{2}+h(\zeta)\right)}{\cos(\zeta)+\sin(z)} - \frac{\sin(\zeta)h'(\zeta)s^{(0)}\left(-\frac{\pi}{2}+h(\zeta)\right)}{\cos(\zeta)-\sin(z)}\right)\mathrm{d}\zeta. \tag{4.49}$$

Using the formulae (2.18), (4.40) and (4.44), we find that,

$$h'(\zeta)s^{(0)}\left(\pm\frac{\pi}{2}+h(\zeta)\right) = -\frac{\sin(\zeta)}{\cos(\zeta)\mp\sin(\theta_{\mathrm{T}})},$$

Downloaded from https://academic.oup.com/imamat/article/85/3/421/5822762 by University of Cambridge user on 21 September 2020

hence

$$q^{(0)}(z) = \frac{1}{2\pi i}\int_{-i\infty}^{i\infty}\left(\frac{\sin^2(\zeta)}{(\cos(\zeta)-\sin(z))(\cos(\zeta)+\sin(\theta_\mathrm{T}))} - \frac{\sin^2(\zeta)}{(\cos(\zeta)+\sin(z))(\cos(\zeta)-\sin(\theta_\mathrm{T}))}\right)\mathrm{d}\zeta. \tag{4.50}$$

This can be evaluated exactly by considering the box contour with the corner points $\zeta = \pm i\infty, -\frac{\pi}{2} \pm i\infty$,

$$\oint = \int_{-i\infty}^{i\infty} - \int_{-\frac{\pi}{2}+i\infty}^{i\infty} - \int_{-\frac{\pi}{2}-i\infty}^{-\frac{\pi}{2}+i\infty} + \int_{-\frac{\pi}{2}-i\infty}^{-i\infty}. \tag{4.51}$$

Obviously, the first integral on the right-hand side of (4.51) is $q^{(0)}(z)$. As $|\mathrm{Im}\{\zeta\}| \to \infty$, the integrand has the leading order behaviour, $O\left(e^{-|\mathrm{Im}\{\zeta\}|}\right)$. This implies that the integrals from $-\frac{\pi}{2} \pm i\infty$ to $\pm i\infty$ are 0. The integrand is antisymmetric about the point $\zeta = -\frac{\pi}{2}$, hence the integral from $-\frac{\pi}{2} - i\infty$ to $-\frac{\pi}{2} + i\infty$ is zero too. Lastly, $\oint$ is equal to the sum of the anticlockwise residues from poles in the strip $\mathrm{Re}\{\zeta\} \in \left(-\frac{\pi}{2}, 0\right)$. The only poles in this strip are located at $\zeta = -\frac{\pi}{2} + z$ and $-\frac{\pi}{2} + \theta_\mathrm{T}$ and their respective residues are,

$$\begin{aligned}
&\frac{1}{2\pi i}\frac{\cos(z)}{\sin(z)+\sin(\theta_\mathrm{T})}, \quad \text{at } \zeta = -\frac{\pi}{2} + z,\\
&-\frac{1}{2\pi i}\frac{\cos(\theta_\mathrm{T})}{\sin(z)+\sin(\theta_\mathrm{T})}, \quad \text{at } \zeta = -\frac{\pi}{2} + \theta_\mathrm{T}.
\end{aligned}$$

Hence $q^{(0)}(z)$ is evaluated to,

$$q^{(0)}(z) = \frac{\cos(z)-\cos(\theta_\mathrm{T})}{\sin(z)+\sin(\theta_\mathrm{T})}, \tag{4.52}$$

which matches exactly with (4.48) with $j = 0$. Assuming that (4.48) is true, we find $s^{(j+1)}(z)$ for $j \geq 0$ by the integral (4.37),

$$\begin{aligned}
s^{(j+1)}(z) = \frac{1}{4\pi i}\int_{-i\infty}^{i\infty}\Bigg(&\frac{\cos(z)}{\cos(\zeta)+\sin(z)}\left[q^{(j)}\left(\frac{\pi}{2}+g(\zeta)\right)+q^{(j)}\left(\frac{\pi}{2}-g(\zeta)\right)\right]\\
&+\frac{\cos(z)}{\cos(\zeta)-\sin(z)}\left[q^{(j)}\left(-\frac{\pi}{2}+g(\zeta)\right)+q^{(j)}\left(-\frac{\pi}{2}-g(\zeta)\right)\right]\Bigg)\mathrm{d}\zeta,
\end{aligned} \tag{4.53}$$

where,

$$\begin{aligned}
q^{(j)}\left(\frac{\pi}{2} \pm g(\zeta)\right) &= -\left(\frac{-1}{g'\left(\frac{\pi}{2}-\theta_\mathrm{I}\right)}\right)^j \frac{\cos(\theta_\mathrm{T}) \pm \sin(g(\zeta))}{\cos(g(\zeta))+\sin(\theta_\mathrm{T})},\\
q^{(j)}\left(-\frac{\pi}{2} \pm g(\zeta)\right) &= \left(\frac{-1}{g'\left(\frac{\pi}{2}-\theta_\mathrm{I}\right)}\right)^j \frac{\cos(\theta_\mathrm{T}) \mp \sin(g(\zeta))}{\cos(g(\zeta))-\sin(\theta_\mathrm{T})}.
\end{aligned}$$

Downloaded from https://academic.oup.com/imamat/article/85/3/421/5822762 by University of Cambridge user on 21 September 2020

Applying the formulae (2.18) and (4.40) will simplify (4.53) to,

$$s^{(j+1)}(z) = \left(\frac{-1}{g'\left(\frac{\pi}{2}-\theta_{\mathrm{I}}\right)}\right)^{j+1} \frac{1}{2\pi i}\int_{-i\infty}^{i\infty}\left(\frac{\cos(z)\cos(\theta_{\mathrm{I}})}{(\cos(\zeta)+\sin(z))(\cos(\zeta)+\sin(\theta_{\mathrm{I}}))}\right.$$
$$\left. - \frac{\cos(z)\cos(\theta_{\mathrm{I}})}{(\cos(\zeta)-\sin(z))(\cos(\zeta)-\sin(\theta_{\mathrm{I}}))}\right)\mathrm{d}\zeta. \tag{4.54}$$

Similarly to (4.50), this can be evaluated exactly by completing the contour via the points $\zeta = -\frac{\pi}{2} \pm i\infty$. As $|\mathrm{Im}\{\zeta\}| \to \infty$, the integrand has the leading order behaviour, $O\left(e^{-3|\mathrm{Im}\{\zeta\}|}\right)$, which implies that the integrals from $-\frac{\pi}{2} \pm i\infty$ to $\pm i\infty$ are 0. The integrand is also antisymmetric about the point $\zeta = -\frac{\pi}{2}$, hence the integral from $-\frac{\pi}{2} - i\infty$ to $-\frac{\pi}{2} + i\infty$ is zero too. Lastly, $\oint$ is equal to the sum of the anticlockwise residues from poles in the strip $\mathrm{Re}\{\zeta\} \in \left(-\frac{\pi}{2}, 0\right)$ which are,

$$-\left(\frac{-1}{g'\left(\frac{\pi}{2}-\theta_{\mathrm{I}}\right)}\right)^{j+1} \frac{1}{2\pi i}\frac{\cos(\theta_{\mathrm{I}})}{\sin(z)-\sin(\theta_{\mathrm{I}})}, \quad \text{at } \zeta = -\frac{\pi}{2} + z,$$
$$\left(\frac{-1}{g'\left(\frac{\pi}{2}-\theta_{\mathrm{I}}\right)}\right)^{j+1} \frac{1}{2\pi i}\frac{\cos(z)}{\sin(z)-\sin(\theta_{\mathrm{I}})}, \quad \text{at } \zeta = -\frac{\pi}{2} + \theta_{\mathrm{I}}.$$

Hence $s^{(j+1)}(z)$ is evaluated to,

$$s^{(j+1)}(z) = \left(\frac{-1}{g'\left(\frac{\pi}{2}-\theta_{\mathrm{I}}\right)}\right)^{j+1} \frac{\cos(z)-\cos(\theta_{\mathrm{I}})}{\sin(z)-\sin(\theta_{\mathrm{I}})}, \tag{4.55}$$

which matches perfectly with (4.46). Lastly, assuming that (4.46) is true, we find $q^{(j)}(z)$ for $j \geq 1$ by the integral (4.30),

$$q^{(j)}(z) = \frac{1}{4\pi i}\int_{-i\infty}^{i\infty}\left(\frac{\sin(\zeta)h'(\zeta)}{\cos(\zeta)+\sin(z)}\left[s^{(j)}\left(\frac{\pi}{2}+h(\zeta)\right) - s^{(j)}\left(\frac{\pi}{2}-h(\zeta)\right)\right]\right.$$
$$\left. - \frac{\sin(\zeta)h'(\zeta)}{\cos(\zeta)-\sin(z)}\left[s^{(j)}\left(-\frac{\pi}{2}+h(\zeta)\right) - s^{(j)}\left(-\frac{\pi}{2}-h(\zeta)\right)\right]\right)\mathrm{d}\zeta, \tag{4.56}$$

where,

$$s^{(j)}\left(\frac{\pi}{2} \pm h(\zeta)\right) = -\left(\frac{-1}{g'\left(\frac{\pi}{2}-\theta_{\mathrm{I}}\right)}\right)^{j} \frac{\cos(\theta_{\mathrm{I}}) \pm \sin(h(\zeta))}{\cos(h(\zeta))-\sin(\theta_{\mathrm{I}})},$$
$$s^{(j)}\left(-\frac{\pi}{2} \pm h(\zeta)\right) = -\left(\frac{-1}{g'\left(\frac{\pi}{2}-\theta_{\mathrm{I}}\right)}\right)^{j} \frac{\pm\sin(h(\zeta)) - \cos(\theta_{\mathrm{I}})}{\cos(h(\zeta))+\sin(\theta_{\mathrm{I}})}.$$

Downloaded from https://academic.oup.com/imamat/article/85/3/421/5822762 by University of Cambridge user on 21 September 2020

After substitution and a little rearrangement, we find that

$$q^{(j)}(z) = \left(\frac{-1}{g'\left(\frac{\pi}{2}-\theta_{\mathrm{I}}\right)}\right)^{j} \frac{1}{2\pi i}\int_{-i\infty}^{i\infty}\left(\frac{\sin(\zeta)\sin(h(\zeta))h'(\zeta)}{(\cos(\zeta)-\sin(z))(\cos(h(\zeta))+\sin(\theta_{\mathrm{I}}))}\right.$$
$$\left. - \frac{\sin(\zeta)\sin(h(\zeta))h'(\zeta)}{(\cos(\zeta)+\sin(z))(\cos(h(\zeta))-\sin(\theta_{\mathrm{I}}))}\right)\mathrm{d}\zeta. \tag{4.57}$$

Together with (2.18) and (4.40), we can simplify (4.57) to,

$$\begin{aligned} q^{(j)}(z) &= \left(\frac{-1}{g'\left(\frac{\pi}{2}-\theta_{\mathrm{I}}\right)}\right)^{j} \frac{1}{2\pi i}\int_{-i\infty}^{i\infty}\left(\frac{\sin^2(\zeta)}{(\cos(\zeta)-\sin(z))(\cos(\zeta)+\sin(\theta_{\mathrm{T}}))}\right. \\ &\quad \left. - \frac{\sin^2(\zeta)}{(\cos(\zeta)+\sin(z))(\cos(\zeta)-\sin(\theta_{\mathrm{T}}))}\right)\mathrm{d}\zeta, \\ &= \left(\frac{-1}{g'\left(\frac{\pi}{2}-\theta_{\mathrm{I}}\right)}\right)^{j} q^{(0)}(z), \end{aligned} \tag{4.58}$$

which matches exactly with (4.48). Equations (4.52), (4.55) and (4.58) prove that the high-contrast iterative scheme is valid for the penetrable half-space problem. Another important aspect to investigate is the convergence of the asymptotic series for this example.

Figure 9 is a set of MATLAB density plots of the exact solution (4.38) and the asymptotic solution (4.43) with an increasing number of components and the parameter values: $k_1 = 1$, $k_2 = 2$, $\lambda = 0.1$ and $\theta_{\mathrm{I}} = \pi/4$. These figures clearly show the convergence of the high-contrast approximation onto the exact solution.

One can show the nature of the convergence of the series more clearly by looking at the summations in (4.42) that clearly converge if $0 < \lambda < g'\left(\frac{\pi}{2}-\theta_{\mathrm{I}}\right)$. Figure 10 (left) shows the convergence of the reflection and transmission coefficients in series form (4.42) to the exact solution as the approximation order increases. Figure 10 (right) shows the absolute error of this convergence as the approximation order increases.

5. Strategies for numerical evaluation

So far, we have defined a high-contrast asymptotic approximation to the penetrable wedge problem and used the Wiener–Hopf technique to find the spectral components in integral form,

$$q^{(j)}(z) = \frac{1}{2\pi i}\int_{-i\infty}^{i\infty} q_{\mathrm{int}}^{(j)}(z,\zeta)\mathrm{d}\zeta, \quad s^{(j+1)}(z) = \frac{1}{2\pi i}\int_{-i\infty}^{i\infty} s_{\mathrm{int}}^{(j+1)}(z,\zeta)\mathrm{d}\zeta, \tag{5.1}$$

Downloaded from https://academic.oup.com/imamat/article/85/3/421/5822762 by University of Cambridge user on 21 September 2020

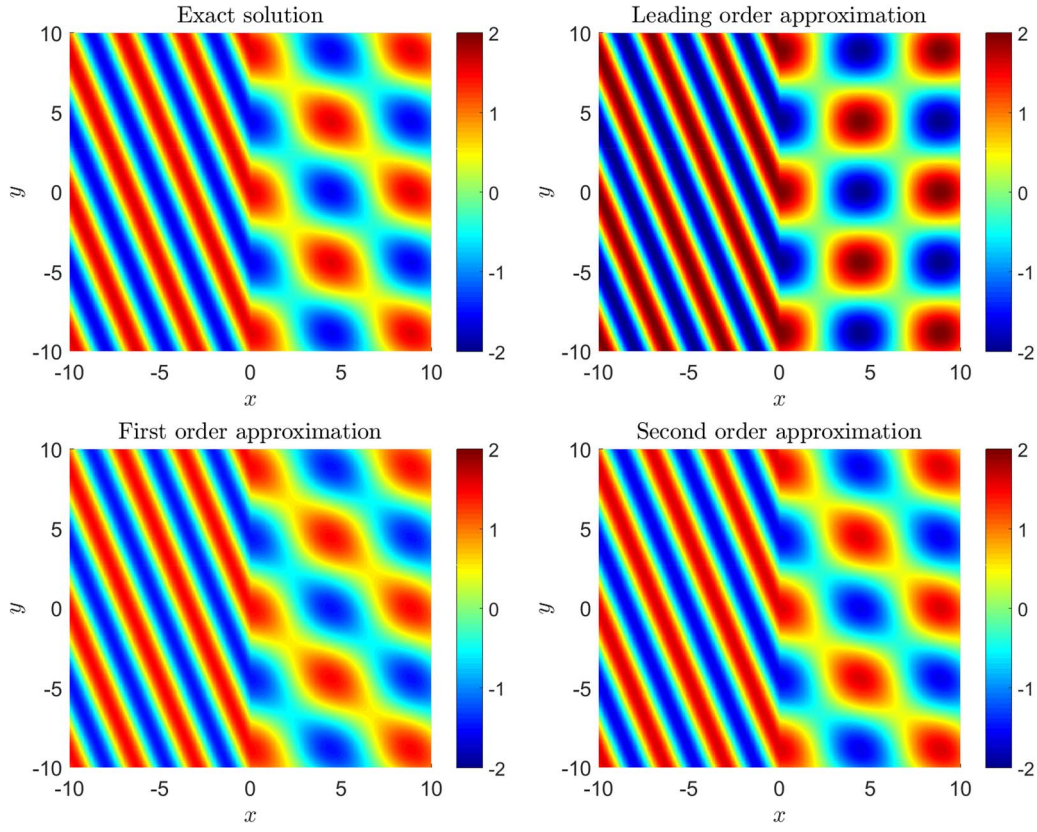

FIG. 9. A comparison of the exact solution (4.38) (upper left) and the asymptotic solution (4.43) including components up to $j = 0$ (upper right), $j = 1$ (lower left) and $j = 2$ (lower right). Here we have $k_1 = 1$, $k_2 = 2$, $\lambda = 0.1$ and $\theta_I = \pi/4$.

where,

$$q_{\text{int}}^{(j)}(z,\zeta) = \frac{\bar{\delta}\sin\left(\bar{\delta}\zeta\right)h'(\zeta)}{2\left(\cos\left(\bar{\delta}\zeta\right)+\sin\left(\bar{\delta}z\right)\right)}\left[s^{(j)}(\theta_w + h(\zeta)) - s^{(j)}(\theta_w - h(\zeta))\right] + \frac{\bar{\delta}\sin\left(\bar{\delta}\zeta\right)h'(\zeta)}{2\left(\cos\left(\bar{\delta}\zeta\right)-\sin\left(\bar{\delta}z\right)\right)}\left[s^{(j)}(-\theta_w - h(\zeta)) - s^{(j)}(-\theta_w + h(\zeta))\right], \tag{5.2}$$

$$s_{\text{int}}^{(j+1)}(z,\zeta) = \frac{\delta\cos\left(\delta z\right)}{2\left(\cos\left(\delta\zeta\right)+\sin\left(\delta z\right)\right)}\left[q^{(j)}(\bar{\theta}_w + g(\zeta)) + q^{(j)}(\bar{\theta}_w - g(\zeta))\right] + \frac{\delta\cos\left(\delta z\right)}{2\left(\cos\left(\delta\zeta\right)-\sin\left(\delta z\right)\right)}\left[q^{(j)}(-\bar{\theta}_w - g(\zeta)) + q^{(j)}(-\bar{\theta}_w + g(\zeta))\right]. \tag{5.3}$$

We have showed the validity of this representation for the half-space case, but now we wish to evaluate it for a more general wedge angle. This situation is much more difficult and the integrals will need to be evaluated numerically. While the integrals (5.1) are valid for any value $\theta_w \in (0,\pi)$, in our

Downloaded from https://academic.oup.com/imamat/article/85/3/421/5822762 by University of Cambridge user on 21 September 2020

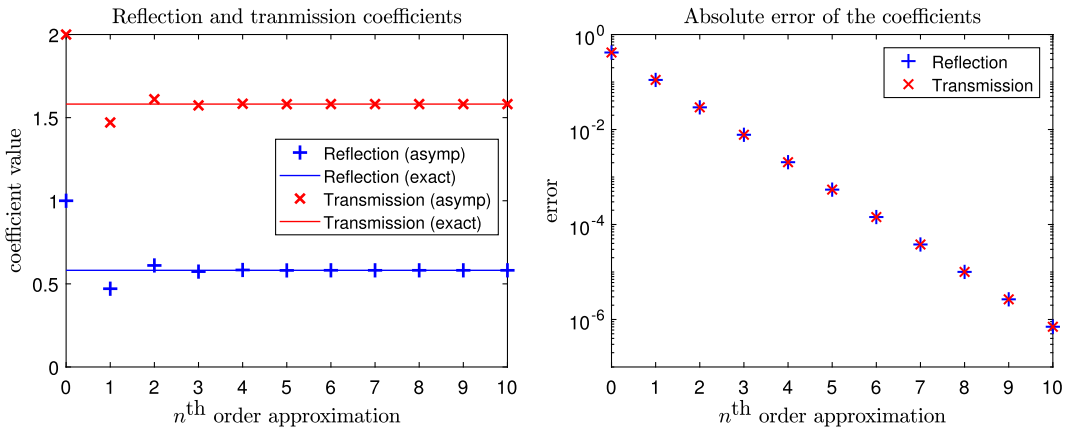

FIG. 10. A comparison between the exact and asymptotic forms of the reflection and transmission coefficients (left) and the absolute error (right) as the approximation order increases. Here we have $k_1 = 1$, $k_2 = 2$, $\lambda = 0.1$ and $\theta_I = \pi/4$.

examples we restrict $\theta_w > \pi/2$ for convenience because the GO component is simpler to find in this configuration.

5.1 *Numerical evaluation of spectral integral*

In order to guarantee accuracy, one must ensure that the integration contour follows a path that does not approach any of the singularities too closely. One way to enforce this is to use an adaptive integration contour (a contour that depends on z) that steers itself around the poles (for example see Fig. 7). In practice however, an integration contour that explicitly depends on z is obviously inefficient. We therefore fix the integration contour to be a straight line with endpoints $\pm i\infty$ but we must still be cautious about singularities.

The branch cuts will not be a concern if we do not consider contour paths going beyond $|\text{Re}\{\zeta\}| = \pi$. This is because, in both (5.2) and (5.3), the cut centred at $\zeta = 0$ has been cancelled out which means that the nearest cuts to the contour are the ones centred at $\zeta = \pm\pi$.

In both integrands, the spectral poles are fixed in place (meaning that their locations are independent of z). The locations and residues of these spectral poles can be found through consideration of the poles of $s^{(0)}(z)$ and the boundary functional conditions (3.18) and (3.25), recalling that $q^{(j)}(z)$ and $s^{(j+1)}(z)$ have pole-free strips (see (3.15), (3.23)). In most cases, these poles are far enough from the contour to not cause any issues. For this reason, we do not discuss these poles in detail here.

The last set of poles (the z-poles) are located at $\zeta = (2n-1)\Theta \pm z$ where $\Theta = \bar{\theta}_w$ or θ_w (for $q^{(j)}(z)$ and $s^{(j+1)}(z)$, respectively) and $n \in \mathbb{Z}$. These poles approach the contour when $\text{Re}\{z\} \to \mp(2n-1)\Theta$. After they cross the contour, their residues will need to be added to retain continuity. For $q^{(j)}_{\text{int}}$, the residues of the poles at $\zeta = (2n-1)\bar{\theta}_w \pm z$ are given by

$$\text{Res}\left(q^{(j)}_{\text{int}}, (2n-1)\bar{\theta}_w \pm z\right) = \frac{1}{2}h'((2n-1)\bar{\theta}_w \pm z)\Big[s^{(j)}(\mp(-1)^n(\theta_w - h((2n-1)\bar{\theta}_w \pm z))) - s^{(j)}(\mp(-1)^n(\theta_w + h((2n-1)\bar{\theta}_w \pm z)))\Big], \tag{5.4}$$

Downloaded from https://academic.oup.com/imamat/article/85/3/421/5822762 by University of Cambridge user on 21 September 2020

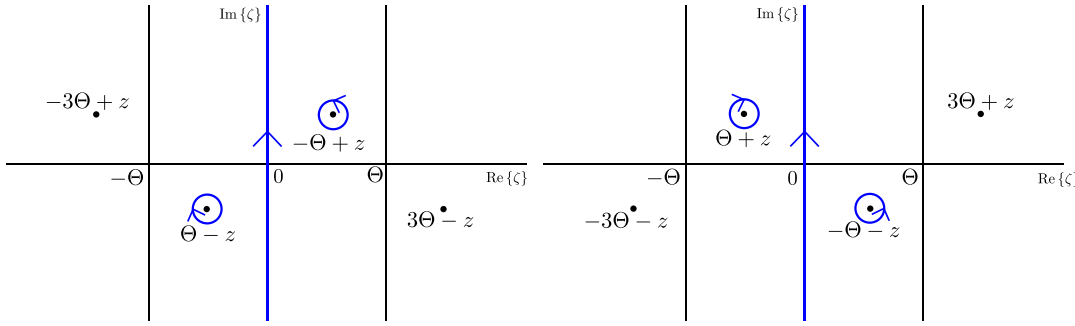

FIG. 11. Diagrams of the ζ-plane for when z-poles have crossed the integration contour. The relevant poles to include are circled for the cases where $\mathrm{Re}\{z\} > \Theta$ (left) and $\mathrm{Re}\{z\} < -\Theta$ (right).

while for $s_{\mathrm{int}}^{(j+1)}$, the residues of the poles at $\zeta = (2n-1)\theta_{\mathrm{w}} \pm z$ are

$$\mathrm{Res}\Big(s_{\mathrm{int}}^{(j+1)}, (2n-1)\theta_{\mathrm{w}} \pm z\Big) = \frac{(-1)^n}{2}\Big[q^{(j)}(\mp(-1)^n\bar{\theta}_{\mathrm{w}} + g((2n-1)\theta_{\mathrm{w}} \pm z)) + q^{(j)}(\mp(-1)^n\bar{\theta}_{\mathrm{w}} - g((2n-1)\theta_{\mathrm{w}} \pm z))\Big]. \tag{5.5}$$

Whenever such a crossing occurs, two poles will cross the contour at the same time in opposite directions due to the evenness of the integrands (see Fig. 11). These poles will have residues that are equal but with opposite sign.

When one of these poles is getting too close to the contour, the numerical integration will begin to lose accuracy. To prevent this, we shall shift the entire integration contour a distance Θ to the right collecting the residues of any crossed poles. This means that we have two cases for evaluation.

$$\text{Original contour: use } \int_{-i\infty}^{i\infty} \quad \text{when} \quad \left(2n-\frac{1}{2}\right)\Theta < \mathrm{Re}\{z\} \le \left(2n+\frac{1}{2}\right)\Theta, \tag{5.6}$$

$$\text{Shifted contour: use } \int_{\Theta-i\infty}^{\Theta+i\infty} \text{ plus residues when } \left(2n+\frac{1}{2}\right)\Theta < \mathrm{Re}\{z\} \le \left(2n+\frac{3}{2}\right)\Theta, \tag{5.7}$$

where $n \in \mathbb{Z}$. The strips in (5.6) are chosen because the local z-poles are closer to the shifted contour than the original (and vice versa for (5.7)). This is demonstrated in Fig. 12 for when $\mathrm{Re}\{z\} \to \Theta^-$. Shifting the contour will cross a single z-pole and at most one spectral pole (likely more if we had $\theta_{\mathrm{w}} < \pi/2$). For $q_{\mathrm{int}}^{(j)}(z)$, the spectral pole is located at $\zeta = g(\theta_{\mathrm{w}} - \theta_{\mathrm{I}})$ (crossed only if $g(\theta_{\mathrm{w}} - \theta_{\mathrm{I}}) < \bar{\theta}_{\mathrm{w}}$) and the value of the residue is,

$$\mathrm{Res}\Big(q_{\mathrm{int}}^{(j)}, g(\theta_{\mathrm{w}} - \theta_{\mathrm{I}})\Big) = \left(\frac{-1}{g'(\theta_{\mathrm{w}} - \theta_{\mathrm{I}})}\right)^j \frac{\bar{\delta}\sin\left(\bar{\delta}g(\theta_{\mathrm{w}} - \theta_{\mathrm{I}})\right)}{\sin(\bar{\delta}z) + \cos\left(\bar{\delta}g(\theta_{\mathrm{w}} - \theta_{\mathrm{I}})\right)}. \tag{5.8}$$

Downloaded from https://academic.oup.com/imamat/article/85/3/421/5822762 by University of Cambridge user on 21 September 2020

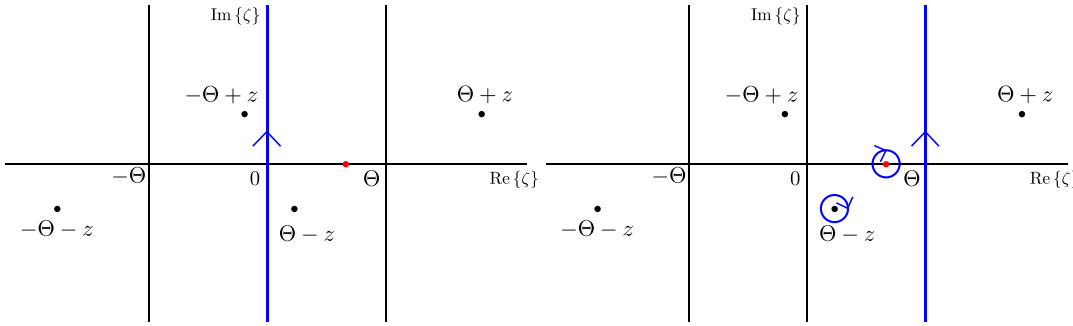

FIG. 12. The ζ-plane diagrams of the original contour (left) versus the shifted contour (right) for when $\Theta/2 < \mathrm{Re}\{z\} < \Theta$. The red dot indicates a potentially crossed spectral pole.

For $s_{\mathrm{int}}^{(j+1)}(z)$, the spectral pole is located at $\zeta = \theta_{\mathrm{w}} - \theta_{\mathrm{I}}$ with the residue value,

$$\mathrm{Res}\left(s_{\mathrm{int}}^{(j+1)}, \theta_{\mathrm{w}} - \theta_{\mathrm{I}}\right) = -\left(\frac{-1}{g'(\theta_{\mathrm{w}} - \theta_{\mathrm{I}})}\right)^{j+1} \frac{\delta \cos(\delta z)}{\sin(\delta z) - \sin\left(\delta\theta_{\mathrm{I}}\right)}. \tag{5.9}$$

For convenience, we define R_{spec} as the spectral pole contribution,

$$R_{\mathrm{spec}} = \begin{cases} \mathcal{H}(\bar{\theta}_{\mathrm{w}} - g(\theta_{\mathrm{w}} - \theta_{\mathrm{I}}))\mathrm{Res}\left(q_{\mathrm{int}}^{(j)}, g(\theta_{\mathrm{w}} - \theta_{\mathrm{I}})\right) & \text{for } q^{(j)}, \\ \mathrm{Res}\left(s_{\mathrm{int}}^{(j+1)}, \theta_{\mathrm{w}} - \theta_{\mathrm{I}}\right) & \text{for } s^{(j+1)}. \end{cases} \tag{5.10}$$

It is important to note that each time the contour is shifted or shifted back, a different z-pole is crossed.

As $|\mathrm{Re}\{z\}|$ becomes larger, identifying which contour to use and calculating the correct residues to add becomes quite tedious. However, one can form functional difference equations from the boundary functional conditions (3.18) and (3.25). These functional equations are used as a method of analytic continuation and take the form,

$$\begin{aligned} q^{(j)}(z) = {} & q^{(j)}(z \pm 4\bar{\theta}_{\mathrm{w}}) - h'(z \pm 3\bar{\theta}_{\mathrm{w}})\left[s^{(j)}(\mp\theta_{\mathrm{w}} + h(z \pm 3\bar{\theta}_{\mathrm{w}})) - s^{(j)}(\mp\theta_{\mathrm{w}} - h(z \pm 3\bar{\theta}_{\mathrm{w}}))\right] \\ & + h'(z \pm \bar{\theta}_{\mathrm{w}})\left[s^{(j)}(\pm\theta_{\mathrm{w}} + h(z \pm \bar{\theta}_{\mathrm{w}})) - s^{(j)}(\pm\theta_{\mathrm{w}} - h(z \pm \bar{\theta}_{\mathrm{w}}))\right], \end{aligned} \tag{5.11}$$

$$\begin{aligned} s^{(j+1)}(z) = {} & s^{(j+1)}(z \pm 4\theta_{\mathrm{w}}) - q^{(j)}(\mp\bar{\theta}_{\mathrm{w}} + g(z \pm 3\theta_{\mathrm{w}})) - q^{(j)}(\mp\bar{\theta}_{\mathrm{w}} - g(z \pm 3\theta_{\mathrm{w}})) \\ & + q^{(j)}(\pm\bar{\theta}_{\mathrm{w}} + g(z \pm \theta_{\mathrm{w}})) + q^{(j)}(\pm\bar{\theta}_{\mathrm{w}} - g(z \pm \theta_{\mathrm{w}})). \end{aligned} \tag{5.12}$$

This allows us to extend a previously defined base strip (that has width $4\bar{\theta}_{\mathrm{w}}$ or $4\theta_{\mathrm{w}}$ for $q^{(j)}(z)$ and $s^{(j+1)}(z)$, respectively) to the entire complex plane (see Fig. 13). These functional equations can be implemented in software such as MATLAB by defining a recursive function. We choose the following

Downloaded from https://academic.oup.com/imamat/article/85/3/421/5822762 by University of Cambridge user on 21 September 2020

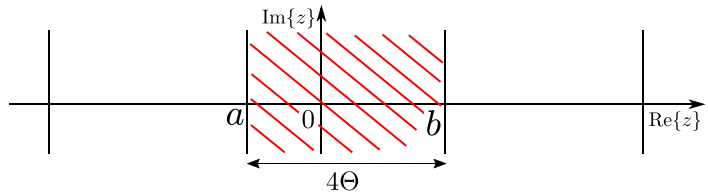

FIG. 13. Demonstration of the functional difference equations. The red region will be the base strip (5.13) with $a = -\frac{3\Theta}{2}$ and $b = \frac{5\Theta}{2}$. Then the adjacent strips will require the functional difference equations in the evaluation.

definition of the base strip for all spectral functions:

$$p(z) = \begin{cases} \dfrac{1}{2\pi i}\displaystyle\int_{\Theta-i\infty}^{\Theta+i\infty} p_{\text{int}}(z,\zeta)\mathrm{d}\zeta - R_{\text{spec}} - \text{Res}(p_{\text{int}}, \Theta + z) & -\frac{3\Theta}{2} < \text{Re}\,\{z\} \le -\frac{\Theta}{2} \quad (5.13a) \\ \dfrac{1}{2\pi i}\displaystyle\int_{-i\infty}^{i\infty} p_{\text{int}}(z,\zeta)\mathrm{d}\zeta & -\frac{\Theta}{2} < \text{Re}\,\{z\} \le \frac{\Theta}{2} \quad (5.13b) \\ \dfrac{1}{2\pi i}\displaystyle\int_{\Theta-i\infty}^{\Theta+i\infty} p_{\text{int}}(z,\zeta)\mathrm{d}\zeta - R_{\text{spec}} - \text{Res}(p_{\text{int}}, \Theta - z) & \frac{\Theta}{2} < \text{Re}\,\{z\} \le \frac{3\Theta}{2} \quad (5.13c) \\ \dfrac{1}{2\pi i}\displaystyle\int_{-i\infty}^{i\infty} p_{\text{int}}(z,\zeta)\mathrm{d}\zeta - 2\text{Res}(p_{\text{int}}, \Theta - z) & \frac{3\Theta}{2} < \text{Re}\,\{z\} \le \frac{5\Theta}{2}, \quad (5.13d) \end{cases}$$

where $\Theta = \bar{\theta}_{\text{w}}$ (resp. θ_{w}) for $p = q^{(j)}$ (resp. $s^{(j+1)}$). Then (5.11) (resp. (5.12)) analytically continue this base strip to the entire z complex plane.

This strategy is complete for $q^{(0)}(z)$ but the higher order integrals are nested integrals because of the spectral functions inside the integrand. Numerical computations of nested integrals are notoriously difficult to evaluate numerically. However a sufficiently accurate approximation can give us a substantially quicker computation without sacrificing too much precision. We will use spline interpolation as detailed in the following steps.

Step 1 Take (5.13) and transform the integrals so that the range is from 0 to ∞, e.g.

$$\frac{1}{2\pi i}\int_{-i\infty}^{i\infty} s_{\text{int}}^{(j)}(z,\zeta)\mathrm{d}\zeta = \frac{1}{\pi}\int_{0}^{\infty} s_{\text{int}}^{(j)}(z,it)\mathrm{d}t. \quad (5.14)$$

Step 2 Identify the spectral parts to interpolate, e.g. the following sections from $s_{\text{int}}^{(j)}(z,it)$:

$$\mathcal{Q}(t) = q^{(j)}(\pm\bar{\theta}_{\text{w}} + g(it)) + q^{(j)}(\pm\bar{\theta}_{\text{w}} - g(it)), \quad (5.15)$$

where $t \in [0,\infty)$.

Step 3 For simplicity, we map these spectral parts onto a unit-sized domain using functions such as,

$$t(\tau) = \frac{\tau}{1-\tau}, \quad \tau \in [0,1). \quad (5.16)$$

Downloaded from https://academic.oup.com/imamat/article/85/3/421/5822762 by University of Cambridge user on 21 September 2020

The ability to do this step is evidenced by knowing that the spectral parts are well behaved at infinity because of the spectral functions asymptotic behaviour from (3.14) and (3.22).

Step 4 Use spline interpolation on a linearly spaced set of τ points to get an accurate numerical result that is continuously differentiable,

$$\widetilde{\mathcal{Q}}(t(\tau)) \approx \mathcal{Q}(t(\tau)). \tag{5.17}$$

Step 5 Invert the unit mapping to go back to the t domain by applying

$$\tau(t) = \frac{t}{1+t}. \tag{5.18}$$

Step 6 Integrate the approximated integrand with $\widetilde{\mathcal{Q}}(t)$ in place of $\mathcal{Q}(t)$.

On a side note, Appendix B can be used to further argue that the ideal unit mapping for $s^{(1)}(z)$ is,

$$t(\tau) = -(1/\delta)\ln(1-\tau), \quad \tau \in [0,1), \tag{5.19}$$

because it implies the following behaviour for $q^{(0)}(z)$ as $\tau \to 1^-$,

$$q^{(0)}(\mathrm{Re}\,\{z\} - (i/\delta)\ln(1-\tau)) = -i\delta + O(1-\tau). \tag{5.20}$$

At the time of writing, ideal unit mappings in the general case have not been found so we will generally use (5.16) in later results.

Concluding this subsection, we have discussed our strategy to efficiently evaluate $q^{(j)}(z)$ and $s^{(j+1)}(z)$ by combining interpolation, two cases of fixed contours and functional difference equations. Figure 14 includes phase portraits of $s^{(0)}(z)$, $q^{(0)}(z)$, $s^{(1)}(z)$ and $q^{(1)}(z)$ with $\lambda_k = 1/2$, $\bar{\theta}_{\mathrm{w}} = \pi/4$ and $\theta_{\mathrm{I}} = \pi/8$ as well as indications of local poles, branch cuts and strips of analyticity.

5.2 *Numerical evaluation of Sommerfeld integrals*

The tools developed for the evaluation of the spectral integrals can be adapted in order to evaluate the Sommerfeld integrals. Recall the two Sommerfeld integral forms of the exterior and interior total wave fields,

$$\Phi(r,\theta) = \frac{1}{2\pi i}\int_{\gamma_+ + \gamma_-} e^{-ik_1 r\cos(z)} s(\theta+z)\mathrm{d}z, \quad \Psi(r,\theta) = \frac{1}{2\pi i}\int_{\gamma_+ + \gamma_-} e^{-ik_2 r\cos(z)} q(\theta-\pi+z)\mathrm{d}z, \tag{5.21}$$

where the Sommerfeld contours $\gamma_\pm$ are displayed in Fig. 3 and the spectral functions $s(z)$ and $q(z)$ have the high-contrast expansion of the form,

$$p(z) = p^{(0)}(z) + \lambda p^{(1)}(z) + \lambda^2 p^{(2)}(z) + O(\lambda^3). \tag{5.22}$$

All singularities in the two integrands are caused by the spectral functions and are confined to the real line and the local vicinity of branch cuts. The branch cuts for Φ are centred on and perpendicular

Downloaded from https://academic.oup.com/imamat/article/85/3/421/5822762 by University of Cambridge user on 21 September 2020

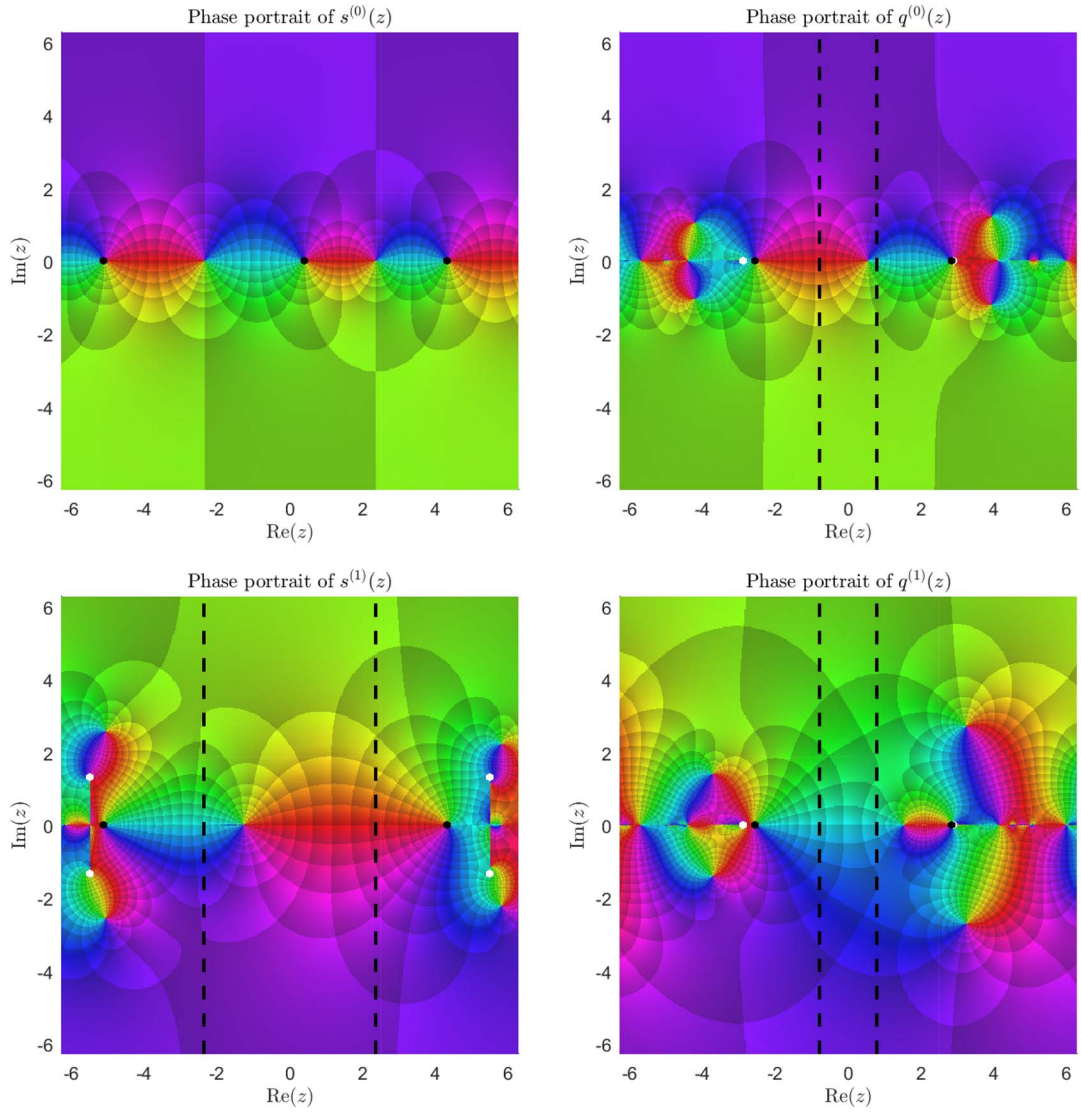

FIG. 14. Phase portraits of $s^{(0)}(z)$ (upper left), $q^{(0)}(z)$ (upper right), $s^{(1)}(z)$ (lower left) and $q^{(1)}(z)$ (lower right) with $\lambda_k = 1/2$, $\bar{\theta}_{\mathrm{w}} = \pi/4$ and $\theta_{\mathrm{I}} = \pi/8$. The black dots indicate the location of local poles and the white dots indicate the location of local branch points. For all portraits minus $s^{(0)}(z)$, the strips of analyticity, (3.15) and (3.23), are between the two dashed lines. See Fig. 1 (right) for colour reference.

to the real line and the branch cuts for Ψ are on the real line. Using Sommerfeld contours for numerical integration is generally impractical because of the highly oscillatory nature of $\exp(-ik_{1,2}r\cos(z))$ when $k_{1,2}r$ is too large.

We deform the Sommerfeld contours to the steepest descent contours using similar methodology to section 5 in Nethercote *et al.* (2020). The deformation crosses all poles on the real line segment

Downloaded from https://academic.oup.com/imamat/article/85/3/421/5822762 by University of Cambridge user on 21 September 2020

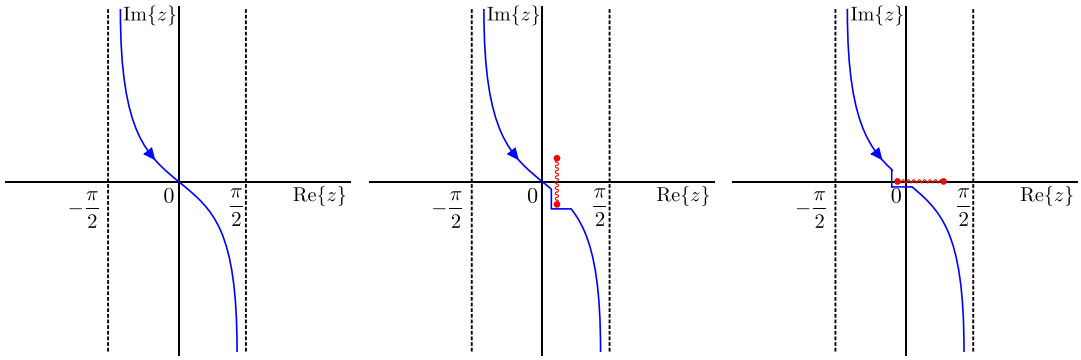

FIG. 15. Illustrations of the steepest descent path (in blue) normally (left) and around the branch cuts for Φ (middle) and Ψ (right).

$z \in [-\pi, \pi]$ except for any poles situated on the branch cuts. These poles create the GO component (at least in part) leaving the steepest descent integral to represent the diffracted component. The deformation reduces the Sommerfeld integral to the form,

$$\Phi(r,\theta) = \Phi_{\text{GO}} + \frac{1}{2\pi i}\int_{\text{SDP}} e^{ik_1 r\cos(z)}\left[s(\theta+\pi+z) - s(\theta-\pi-z)\right]\mathrm{d}z, \tag{5.23}$$

$$\Psi(r,\theta) = \Psi_{\text{GO}} + \frac{1}{2\pi i}\int_{\text{SDP}} e^{ik_2 r\cos(z)}\left[q(\theta+z) - q(\theta-2\pi-z)\right]\mathrm{d}z, \tag{5.24}$$

where SDP is the steepest descent path shown in Fig. 15 (left). The SDP is parameterized in terms of the Gudermannian function $\text{gd}(x)$,

$$z(t) = t - \text{gd}(it) = t - i\ln\left|\sec(t) + \tan(t)\right|, \quad t \in \left(-\frac{\pi}{2}, \frac{\pi}{2}\right), \tag{5.25}$$

and has the properties,

$$\frac{\mathrm{d}z}{\mathrm{d}t} = 1 - i\sec(t), \quad \cos(z(t)) = 1 + i\sin(t)\tan(t), \tag{5.26}$$

the latter of which shows that along this path of steepest descent the exponential part $\exp(-ik_{1,2}r\cos(z))$ does not oscillate at all. GO discontinuities are produced when poles cross the steepest descent path, causing potential numerical issues.

The branch cuts in the spectral functions are another complication to consider. They will eventually intersect the SDP when θ is close to the wedge faces and we need to deform the SDP around the cuts to account for their contribution (see Fig. 15 (middle) for the Φ Sommerfeld integral and Fig. 15 (right) for the Ψ Sommerfeld integral). This contribution produces head/lateral waves that enforce continuity of the diffracted component across the wedge faces.

For Φ, one of the branch cuts is located at

$$z = \theta_{\text{w}} - \theta + iy, \quad \text{where} \quad y \in \left[-\cosh^{-1}\left(\frac{1}{\lambda_k}\right), \cosh^{-1}\left(\frac{1}{\lambda_k}\right)\right], \tag{5.27}$$

Downloaded from https://academic.oup.com/imamat/article/85/3/421/5822762 by University of Cambridge user on 21 September 2020

and intersects the contour when $\theta_w - \cos^{-1}(\lambda_k) \leq \theta \leq \theta_w$. There is also a second cut located at

$$z = \theta_w + \theta + iy, \quad \text{where} \quad y \in \left[-\cosh^{-1}\left(\frac{1}{\lambda_k}\right), \cosh^{-1}\left(\frac{1}{\lambda_k}\right) \right], \tag{5.28}$$

and intersects the contour when $-\theta_w \leq \theta \leq -\theta_w + \cos^{-1}(\lambda_k)$. Equation (5.23) does have more branch cuts but these will not intersect the contour.

For Ψ, one of the branch cuts is located at

$$z = \theta - \theta_w + x, \quad \text{where} \quad x \in \left[-\cos^{-1}\left(\lambda_k\right), \cos^{-1}\left(\lambda_k\right) \right], \tag{5.29}$$

and intersects the contour when $\theta_w \leq \theta \leq \theta_w + \cos^{-1}(\lambda_k)$. A second cut is located at

$$z = \pi + \bar{\theta}_w - \theta + x, \quad \text{where} \quad x \in \left[-\cos^{-1}\left(\lambda_k\right), \cos^{-1}\left(\lambda_k\right) \right], \tag{5.30}$$

and intersects the contour when $\pi + \bar{\theta}_w - \cos^{-1}\left(\lambda_k\right) \leq \theta \leq \pi + \bar{\theta}_w$. Equation (5.24) also has other inconsequential branch cuts that need not be considered. When numerically integrating, we should indent the contour so that the cuts are avoided.

Lastly, we reuse interpolation in the evaluation of Sommerfeld integrals, specifically on the spectral parts e.g. $s(\theta + \pi + z) - s(\theta - \pi - z)$. Similarly to the spectral integrals, we use a linearly spaced set of points and spline interpolation to create an accurate approximation that allows the integration to be substantially faster without sacrificing too much precision. Although this time, we will need some two-dimensional interpolations (e.g. θ and z parameterized by (5.25)).

5.3 *Numerical examples and comparisons*

Combining all the strategy components from the previous two subsections completes our method of evaluation for both the exterior and interior total wave fields. This works very well in most cases although one should be careful to include the correct GO poles. Because the integration is along the steepest descent contours, the value of $k_{1,2}r$ does not affect the computation speed much except for extreme cases. Before we conclude this article, we will define and evaluate four different test cases using the discussed strategies, discuss the convergence of the asymptotic series and compare with existing literature.

For all test cases, we will consider a right-angled wedge. The parameter values for the four test cases are defined in Table 1. The first two test cases will have both wedge faces illuminated by the incident wave creating a reflected and transmitted wave per face. The difference between these two test cases is the value of the contrast parameter. The other two test cases will have just the top face illuminated, creating a single reflection and transmission. For test case 3, this transmitted wave will also be totally reflected upon impact with the bottom face. For test case 4, the scatterer wavenumber is smaller, hence the transmitted wave will be internally reflected and retransmitted through the bottom face.

Figure 16 shows some polar plots of the total field's magnitude at $r = 5$ for all test cases using the asymptotic series with terms up to and including $j = 0,\ 1,\ 2$ and 3. Note that the approximate fields shown in Fig. 16 contain all the expected physical components of the wave field, including head/lateral waves. All figures show converging behaviour as the order of the approximation increases and these

Downloaded from https://academic.oup.com/imamat/article/85/3/421/5822762 by University of Cambridge user on 21 September 2020

TABLE 1 *Table of parameter values for the four different test cases*

Test case	$\bar{\theta}_w$	θ_I	k_1	k_2	λ
1	$\pi/4$	$\pi/8$	1	2	0.1
2	$\pi/4$	$\pi/8$	1	2	0.01
3	$\pi/4$	$\pi/2$	1	2	0.1
4	$\pi/4$	$\pi/2$	1	1.2	0.1

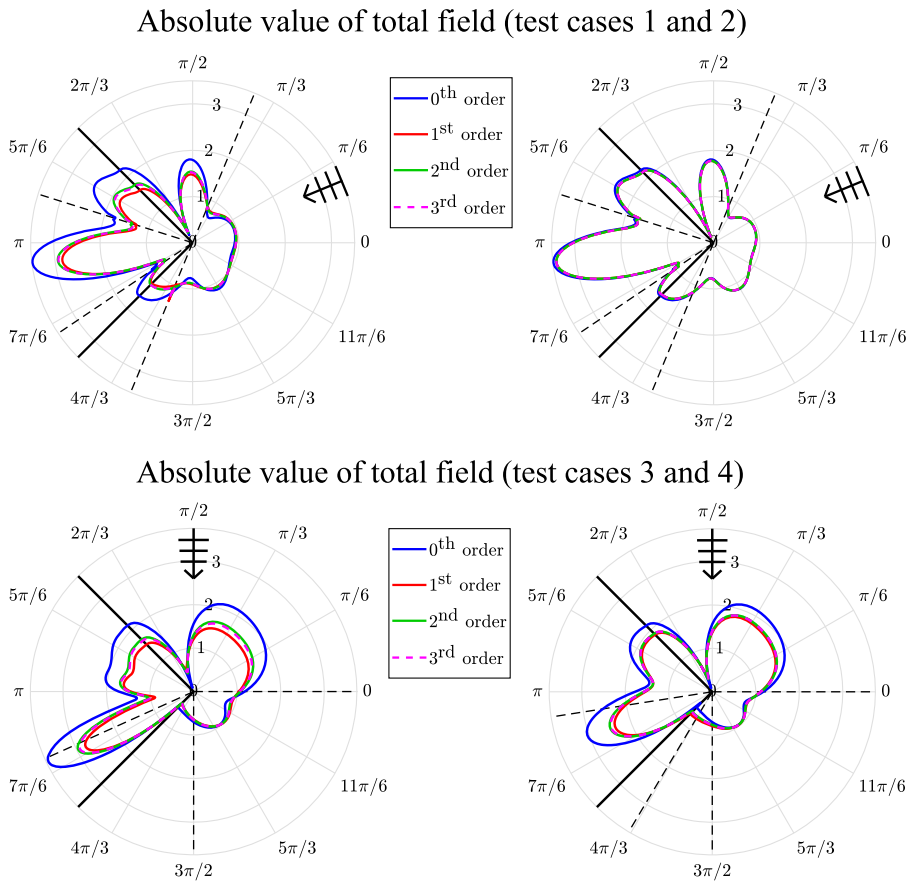

FIG. 16. Polar plots of the total field's magnitude at $r = 5$ where the approximation order goes up to and including $j = 3$. Each graph represents a different test case: 1 (upper left), 2 (upper right), 3 (lower left) and 4 (lower right).

results have also been compared to (and agree with) those calculated using the finite element software COMSOL MultiPhysics version 5.3 (see Fig. 17).

It is clear that test case 2 (with a smaller λ) converges much faster and one can see the extra retransmitted wave in test case 4 compared with test case 3. These plots also indicate the locations of the incident wave and GO discontinuities, where one can notice, when looking closely, small numerical

Downloaded from https://academic.oup.com/imamat/article/85/3/421/5822762 by University of Cambridge user on 21 September 2020

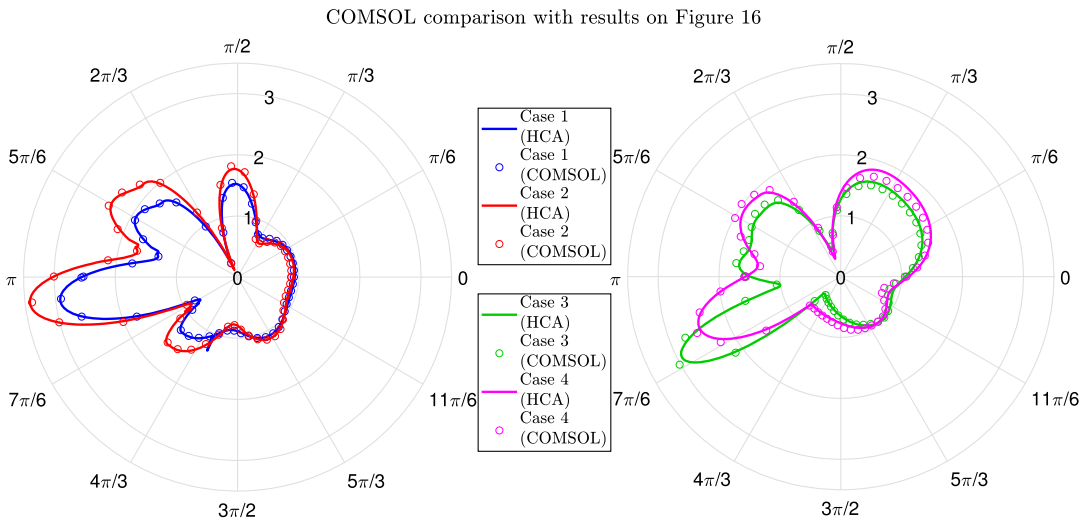

FIG. 17. Polar plot comparison of our best results from Fig. 16 with the solution obtained by COMSOL MultiPhysics. Here we plot the 3rd order approximations at $r = 5$ for all test cases (see Table 1 for parameter values).

inaccuracies. These are due to the fact that in this case, the contour of integration is very near a pole. Automated deformation of the contour would solve this issue, but we do not do it here for brevity.

In the process of creating our numerical results, we analysed the accuracy by investigating the error of the individual interpolations and we checked that the boundary functional conditions (given by (3.18) and (3.25)) are satisfied by inputting the numerical data of the spectral functions. We can also check the convergence of the asymptotic series by considering the error in the interface conditions. Since we truncate both the exterior and interior asymptotic series at the same point, the Dirichlet interface conditions are automatically satisfied, hence we consider the error in the Neumann interface conditions. Applying the high-contrast approximation (truncated at j) and considering the boundary conditions of the individual components simplifies the Neumann interface conditions to

$$\left.\frac{\partial \Phi}{\partial \theta}\right|_{\theta=\pm\theta_{\mathrm{w}}} - \lambda \left.\frac{\partial \Psi}{\partial \theta}\right|_{\theta=\pi\mp\bar{\theta}_{\mathrm{w}}} = -\lambda^{j+1} \left.\frac{\partial \Psi^{(j)}}{\partial \theta}\right|_{\theta=\pi\mp\bar{\theta}_{\mathrm{w}}}. \tag{5.31}$$

We put the θ derivative in Sommerfeld integral form,

$$-\lambda^{j+1} \left.\frac{\partial \Psi^{(j)}}{\partial \theta}\right|_{\theta=\pi\mp\bar{\theta}_{\mathrm{w}}} = \frac{\lambda^{j+1} k_2 r}{2\pi} \int_{\gamma_+ + \gamma_-} \sin(z) e^{-ik_2 r\cos(z)} q^{(j)}(\mp\bar{\theta}_{\mathrm{w}} + z)\mathrm{d}z, \tag{5.32}$$

and use the same strategies outlined in Section 5.2 to evaluate these quantities. Figure 18 plots the absolute values of (5.31) with respect to r for test case 1. This figure clearly shows the error decreasing as the order of the approximation increases.

Finally, we shall compare our solution with the uniform far-field formula stated in section 4.5 of Lyalinov (1999) because this paper features a similar high-contrast approximation to ours. Although this formula was stated to be uniform with respect to θ, there seems to be an invalid point at $\theta = \theta_{\mathrm{I}} - \pi$.

Downloaded from https://academic.oup.com/imamat/article/85/3/421/5822762 by University of Cambridge user on 21 September 2020

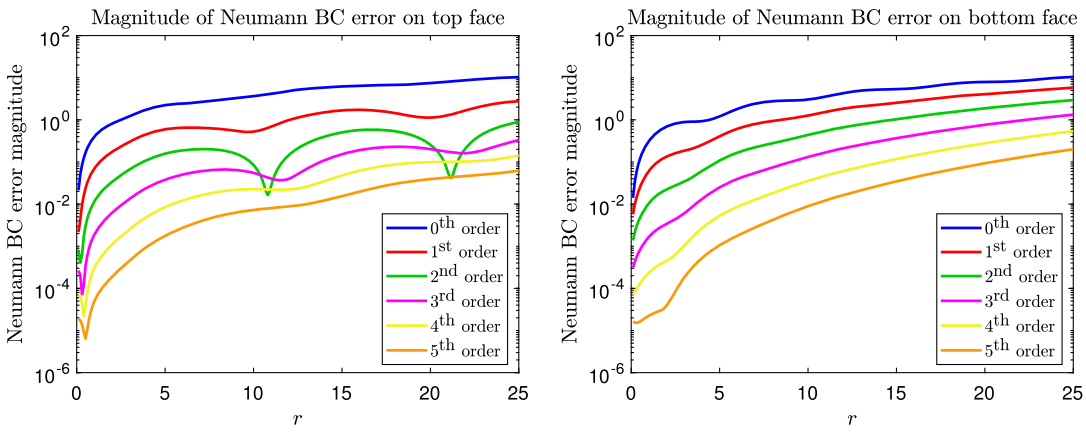

FIG. 18. Plots of the absolute values of (5.31) for test case 1 including the leading order to the fifth order approximations.

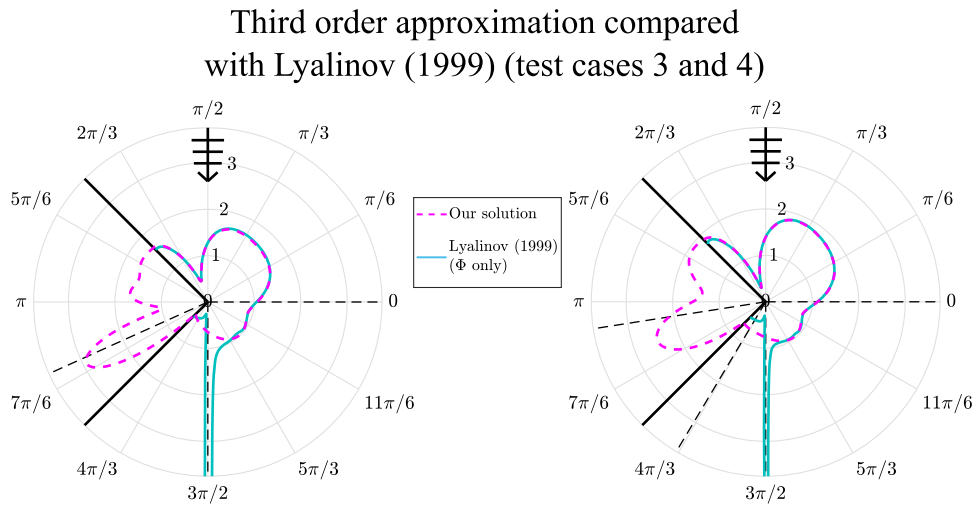

FIG. 19. Polar plot comparison of our third order approximation with the solution from Lyalinov (1999) at $r = 5$ for test cases 3 (left) and 4 (right).

It was also stated that this formula neglects the effect of the branch cuts in the spectral functions (which give rise to head/lateral waves) and because it is leading order, retransmitted waves do not appear either.

Figure 19 compares the third order approximation of test cases 3 and 4 with Lyalinov's far-field approximation. These figures show that there is clear agreement between the two solutions for most values of θ, the exceptions being at the singularity $\theta = \theta_{\text{I}} - \pi$ and some approximation inaccuracies at the wedge faces. We mentioned earlier that Lyalinov does not include retransmitted waves in the final formula, hence there is disagreement in test case 4 by the bottom wedge face.

Downloaded from https://academic.oup.com/imamat/article/85/3/421/5822762 by University of Cambridge user on 21 September 2020

TABLE 2 *Table of times to define the components and the interpolations required for test case 1. Note that these times are approximate*

Approximation order	Spectral functions	Wave fields
0	$<$ 1 second	30 seconds
1	20 seconds	5 minutes
2	2 minutes	35 minutes
3	8 minutes	180 minutes

5.4 *Concluding remarks*

To summarize this article, we created an asymptotic approximation to the penetrable wedge problem with the assumption of high contrast between the host and the scatterer. This assumption split the problem into an infinite set of impenetrable wedge problems that were solved individually using a combination of the Sommerfeld–Malyuzhinets and Wiener–Hopf techniques. We also checked the solution analytically with the penetrable half-space problem and discussed our numerical evaluation strategy of the resulting integral solutions.

For our computations, we used MATLAB R2017a on a desktop with an Intel quad-core CPU @ 3.2 GHz 8GB RAM. Table 2 illustrates the computation times to define the individual components of the high-contrast approximation. It is important to note that these times are approximate and only account for the definitions of the components and the interpolations required assuming that all previous ones have already been made.

Although the polar plots in Fig. 16 show that our method can create an efficient and accurate solution, there are some drawbacks. Generally, the strategies discussed in Section 5 work for a wide range of parameters provided λ is sufficiently small but will struggle for extreme cases such as grazing incidence ($\theta_{\mathrm{I}} \to \theta_{\mathrm{w}}$) and thin wedges ($\bar{\theta}_{\mathrm{w}} \to 0$). In the grazing incidence case, some of the spectral poles will approach the end points of the spectral integration contour causing potential numerical issues. The thin wedge case can be difficult because the z-poles become dense and approach the spectral integration contour on two sides.

Improvements could be made to the numerical strategies such as, defining the ideal unit mapping for the interpolations of the spectral functions by using the Lambert W function or using asymptotic approaches to account for branch cut contributions in the Sommerfeld integrals. It may also be worth investigating the convergence of the asymptotic scheme more rigorously because it could lead to a condition for convergence (e.g. recall $0 < \lambda < g'\left(\frac{\pi}{2} - \theta_{\mathrm{I}}\right)$ for the penetrable half-space) or finding an approximation for the error in case of convergence.

Because it is difficult to numerically compute Sommerfeld integrals when kr is too large, one future task is to create a simple high-frequency/far-field approximation that truly is uniform with respect to θ, which will allow us to efficiently predict the diffraction coefficient of the problem. This will require us to apply the method of steepest descent to Sommerfeld integrals; however, this case is more complicated due to the branch cuts. Obtaining this formula requires us to accurately approximate the branch cut integrals. A high-frequency/far-field approximation will be useful in hybrid numerical-asymptotic approaches for convex polygon diffraction (see Groth *et al.*, 2018).

Recall that in this article, we assumed that the physical parameters are independent of each other. If we were to relax this particular assumption, then in both acoustic and electromagnetic settings we find that the refractive index and the contrast parameter could be connected by $\lambda_k \propto \sqrt{\lambda}$. We will explore how this can affect our method in future work.

Downloaded from https://academic.oup.com/imamat/article/85/3/421/5822762 by University of Cambridge user on 21 September 2020

Funding

Engineering and Physical Sciences Research Council (EPSRC) (DTA studentship to M.A.N., EP/N013719/1 to R.C.A.) and Engineering and Physical Sciences Research Council/United Kingdom Research and Innovation (EPSRC/UKRI) (EP/K032208/1 and EP/R014604/1 to I.D.A.).

References

Abramowitz, M. & Stegun, I. A. (1967) *Handbook of Mathematical Functions: With Formulas, Graphs and Mathematical Tables*, 6th edn. Washington, D.C.: National Bureau of Standards.

Assier, R. C. & Abrahams, I. D. (2019) A surprising observation on the quarter-plane diffraction problem. arXiv:1905.03863.

Assier, R. C. & Shanin, A. V. (2019) Diffraction by a quarter-plane. Analytical continuation of spectral functions. *Q. J. Mech. Appl. Math.*, **72**, 51–86.

Babich, V. M., Lyalinov, M. A. & Grikurov, V. E. (2007) *Diffraction Theory: The Sommerfeld-Malyuzhinets Technique (Alpha Science Series on Wave Phenomena)*. Oxford: Alpha Science.

Babich, V. M. & Mokeeva, N. V. (2008) Scattering of the plane wave by a transparent wedge. *J. Math. Sci.*, **155**, 335–342.

Babich, V. M., Mokeeva, N. V. & Samokish, B. A. (2012) The problem of scattering of a plane wave by a transparent wedge: a computional approach. *J. Commun. Technol. Electron.*, **57**, 993–1000.

Bender, C. M. & Orszag, S. A. (1999) *Advanced Mathematical Methods for Scientists and Engineers I: Asymptotic Methods and Perturbation Theory*. New York: Springer.

Bowman, J. J., Senior, T. B. A. & Uslenghi, P. L. E. (1987) *Electromagnetic and Acoustic Scattering by Simple Shapes*. New York: Hemisphere Publishing Corporation.

Budaev, B. V. (1995) *Diffraction by Wedges* (Pitman Research notes in Mathematics volume 322). Essex: Longman Scientific and Technical.

Budaev, B. V. & Bogy, D. B. (1995) Rayleigh wave scattering by a wedge. *Wave Motion*, **22**, 239–257.

Budaev, B. V. & Bogy, D. B. (1996) Rayleigh wave scattering by a wedge II. *Wave Motion*, **24**, 307–314.

Budaev, B. V. & Bogy, D. B. (1998) Rayleigh wave scattering by two adhering elastic wedges. *Proc. R. Soc. A*, **454**, 2949–2996.

Budaev, B. V. & Bogy, D. B. (1999) Rigorous solutions of acoustic wave diffraction by penetrable wedges. *J. Acoust. Soc. Am.*, **105**, 74–83.

Chandler-Wilde, S. N., Graham, I. G., Langdon, S. & Spence, E. A. (2012) Numerical-asymptotic boundary integral methods in high-frequency acoustic scattering. *Acta Numerica*, **21**, 89–305.

Croisille, J.-P. & Lebeau, G. (1999) *Diffraction by an Immersed Elastic Wedge*. Berlin: Springer.

Daniele, V. G. (2003a) Rotating waves in the Laplace domain for angular regions. *Electromagnetics*, **23**, 223–236.

Daniele, V. G. (2003b) The Wiener–Hopf technique for impenetrable wedges having arbitrary aperture angle. *SIAM J. Appl. Math.*, **63**, 1442–1460.

Daniele, V. G. (2010) The Wiener–Hopf formulation of the penetrable wedge problem: part I. *Electromagnetics*, **30**, 625–643.

Daniele, V. G. (2011) The Wiener–Hopf formulation of the penetrable wedge problem: part II. *Electromagnetics*, **31**, 1–17.

Daniele, V. G. & Lombardi, G. (2006) Wiener–Hopf solution for impenetrable wedges at skew incidence. *IEEE Trans. Antennas Propag.*, **54**, 2472–2485.

Daniele, V. G. & Lombardi, G. (2007) Fredholm factorization of Wiener–Hopf scalar and matrix kernels. *Radio Sci.*, **42**, 1–19.

Daniele, V. G. & Lombardi, G. (2011) The Wiener–Hopf solution of the isotropic penetrable wedge problem: diffraction and total field. *IEEE Trans. Antennas Propag.*, **59**, 3797–3818.

Daniele, V. G., Lombardi, G. & Zich, R. S. (2017a) Network representations of angular regions for electromagnetic scattering. *PLoS One*, **12**, 1–53.

Downloaded from https://academic.oup.com/imamat/article/85/3/421/5822762 by University of Cambridge user on 21 September 2020

DANIELE, V. G., LOMBARDI, G. & ZICH, R. S. (2017b) The electromagnetic field for a PEC wedge over a grounded dielectric slab: 1. Formulation and validation. *Radio Sci.*, **52**, 1472–1491.

DANIELE, V. G., LOMBARDI, G. & ZICH, R. S. (2017c) The electromagnetic field for a PEC wedge over a grounded dielectric slab: 2. Diffraction, modal field, surface waves, and leaky waves. *Radio Sci.*, **52**, 1492–1509.

DANIELE, V. G., LOMBARDI, G. & ZICH, R. S. (2018) The double PEC wedge problem: diffraction and total far field. *IEEE Trans. Antennas Propag.*, **66**, 6482–6499.

GROTH, S. P., HEWETT, D. P. & LANGDON, S. (2015) Hybrid numerical-asymptotic approximation for high-frequency scattering by penetrable convex polygons. *IMA J. Appl. Math.*, **80**, 324–353.

GROTH, S. P., HEWETT, D. P. & LANGDON, S. (2018) A high frequency boundary element method for scattering by penetrable convex polygons. *Wave Motion*, **78**, 32–53.

KELLER, J. B. (1962) Geometrical theory of diffraction. *J. Opt. Soc. Am.*, **52**, 116–130.

KIRCHHOFF, G. (1883) Zur theorie der lichtstrahlen. *Ann. Phys.*, **254**, 663–695.

KNOPOFF, L. (1969) Elastic wave Propagation in a wedge. *Wave Propagation in Solids* (J. MIKLOWITZ ed.). Los Angeles: ASME, pp. 3–43.

KONTOROVICH, M. J. & LEBEDEV, N. N. (1939) On a method of solution of some problems of the diffraction theory. *J. Phys. (Academy Sci. U.S.S.R.)*, **1**, 229–241.

KOUYOUMJIAN, R. G. & PATHAK, P. H. (1974) A uniform GTD for an edge in a perfectly conducting surface. *Proc. IEEE*, **62**, 1448–1461.

KRAUT, E. A. & LEHMAN, G. W. (1969) Diffraction of electromagnetic waves by a right-angle dielectric wedge. *J. Math. Phys.*, **10**, 1340–1348.

LARSEN, J. (1981) Diffraction of elastic waves by a rigid wedge. *Proc. R. Soc. A*, **376**, 609–617.

LAWRIE, J. B. & ABRAHAMS, I. D. (2007) A brief historical perspective of the Wiener–Hopf technique. *J. Engrg. Math.*, **59**, 351–358.

LYALINOV, M. A. (1999) Diffraction by a highly contrast transparent wedge. *J. Phys. A. Math. Gen.*, **32**, 2183–2206.

MACDONALD, H. M. (1902) *Electric Waves*. Cambridge: Cambridge University Press.

MALYUZHINETS, G. D. (1958a) Excitation, reflection and emission of surface waves from a wedge with given face impedances. *Sov. Phys. Dokl.*, **3**, 752–755.

MALYUZHINETS, G. D. (1958b) Inversion formula for Sommerfeld integral. *Sov. Phys. Dokl.*, **3**, 52–56.

MOKEEVA, N. V. (2006) On the well-posedness of diffraction problems for angular domains. *J. Math. Sci.*, **138**, 5555–5564.

MOKEEVA, N. V. (2007) The limiting absorption principle in the problem of a transparent wedge. *J. Math. Sci.*, **142**, 2597–2604.

NETHERCOTE, M. A. (2019) Effective analytic and asymptotic procedures for wave diffraction by perfect and penetrable wedges. *Ph.D. Thesis*, *University of Manchester*.

NETHERCOTE, M. A., ASSIER, R. C. & ABRAHAMS, I. D. (2020) Analytical methods for perfect wedge diffraction: a review. *Wave Motion*, **93** (102479), 1–36.

NOBLE, B. (1958) *Methods Based on the Wiener–Hopf Technique for the Solution of Partial Differential Equations (1988 reprint)*. New York: Chelsea Publishing Company.

RADLOW, J. (1964) Diffraction by a right-angled dielectric wedge. *Internat. J. Engrg. Sci.*, **2**, 275–290.

RAWLINS, A. D. (1977) Diffraction by a dielectric wedge. *J. Inst. Math. its Appl.*, **19**, 261–279.

RAWLINS, A. D. (1999) Diffraction by, or diffusion into, a penetrable wedge. *Proc. R. Soc. A*, **455**, 2655–2686.

SENIOR, T. B. A. (1959) Diffraction by an imperfectly conducting wedge. *Comm. Pure Appl. Math.*, **12**, 337–372.

SHANIN, A. V. (1996) On wave excitation in a wedge-shaped region. *Acoust. Phys.*, **42**, 612–617.

SHANIN, A. V. (1998) Excitation of waves in a wedge-shaped region. *Acoust. Phys.*, **44**, 592–597.

SMITH, H. R., WEBB, A., CONNOLLY, P. & BARAN, A. J. (2015) Cloud chamber laboratory investigations into the scattering properties of hollow ice particles. *J. Quant. Spectrosc. Radiat. Transf.*, **157**, 106–118.

SOMMERFELD, A. (1896) Mathematische theorie der diffraction. *Math. Ann. (in German)*, **47**, 317–374.

SOMMERFELD, A. (1901) Theoretisches über die Beugung der Röntgenstrahlen. *Z. Angew Math. Phys. (in German)*, **46**, 11–97.

SOMMERFELD, A. (1954) *Optics*. New York: Academic Press.

Downloaded from https://academic.oup.com/imamat/article/85/3/421/5822762 by University of Cambridge user on 21 September 2020

SOMMERFELD, A. (2003) *Mathematical Theory of Diffraction*. Boston: Birkhauser.
UFIMTSEV, P. Y. (2014) *Fundamentals of the Physical Theory of Diffraction*, 2nd edn. New Jersey: John Wiley & Sons.
VAN BLADEL, J. G. (2006) *Electromagnetic Fields*, 2nd edn. New Jersey: John Wiley & Sons.
WEGERT, E. (2012) *Visual Complex Functions*. Basel: Birkhauser.
WIENER, N. & HOPF, E. (1931) Über eine klasse singulärer integralgleichungen. *Sitzungsberichte der Preussischen Akademie der Wissenschaften, Physikalisch-Mathematische Klasse (in German)*, **31**, 696–706.
WILLIAMS, W. E. (1959) Diffraction of an E-polarized plane wave by an imperfectly conducting wedge. *Proc. R. Soc. A*, **252**, 376–393.

A. An important mapping to connect two Sommerfeld integrals

In this section, we will define the mapping $g(z)$ and the associated inverse $h(z)$ to connect the two Sommerfeld integrals (2.16) and (2.17) by the identities (2.18). We need to be cautious so that software such as MATLAB/Mathematica can evaluate these mappings with the correct branch cut orientations. Consider the following definitions:

$$g(z) = \cos^{-1}\left(\lambda_k \cos(z)\right), \quad h(z) = \cos^{-1}\left(\lambda_k^{-1} \cos(z)\right), \tag{A.1}$$

where $\lambda_k = k_1/k_2 \in (0, 1)$. Both the mappings have an infinite number of branch points and branch cuts. For $g(z)$, the branch points are located at, $z = \pm i \cosh^{-1}\left(\lambda_k^{-1}\right) + n\pi$ and for $h(z)$, they are located at, $z = \pm \cos^{-1}\left(\lambda_k\right) + n\pi$ where $n \in \mathbb{Z}$. By default, MATLAB joins these branch points via complex infinity (shown as phase portraits in Figs A20a and A20b with $\lambda_k = 1/2$).

As it stands these definitions are not useful since the branch cuts restrict much of the domain and limit the use of integration contours (e.g. Sommerfeld contours). Ideally, we want the mapping to be as similar to an identity map as possible. This will result in both mappings satisfying several different properties.

- $f(-z) = -f(z)$,
- $f(z^*) = (f(z))^*$ where z^* is the complex conjugate of z,
- $f(z + n\pi) = f(z) + n\pi$, for all $n \in \mathbb{Z}$,
- $f(z) \sim z$ as $\mathrm{Im}\{z\} \to \pm\infty$,

where f could be either g or h.

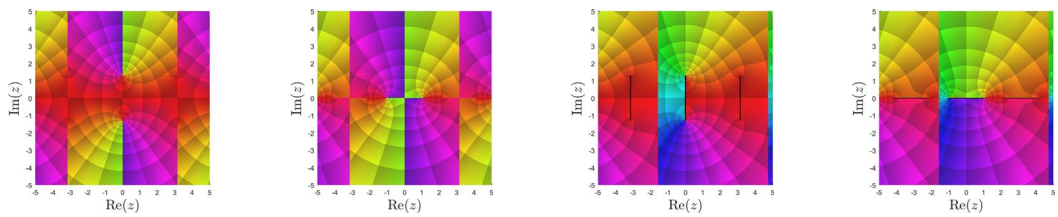

(a) Default definition of $g(z)$ (b) Default definition of $h(z)$ (c) Our definition of $g(z)$ (d) Our definition of $h(z)$

FIG. A20. Phase plots of $g(z)$ and $h(z)$ with the default definition and our definition of the branch cuts (with $\lambda_k = 1/2$). In figure (c) and (d), the black lines indicate the branch cuts. See Fig. 1 (right) for colour reference.

Downloaded from https://academic.oup.com/imamat/article/85/3/421/5822762 by University of Cambridge user on 21 September 2020

For $g(z)$, the branch cuts should be defined to join $z = i\cosh^{-1}\left(\lambda_k^{-1}\right) + n\pi$ and $z = -i\cosh^{-1}\left(\lambda_k^{-1}\right) + n\pi$ via $z = n\pi$ for all $n \in \mathbb{Z}$ and for $h(z)$, the branch cuts should be defined to join $z = \cos^{-1}\left(\lambda_k\right) + n\pi$ and $z = -\cos^{-1}\left(\lambda_k\right) + n\pi$ via $z = n\pi$ for all $n \in \mathbb{Z}$. We use the logarithmic formula for inverse cosine to manipulate the branch cuts,

$$g(z) = \frac{\pi}{2} + i\ln\left(i\lambda_k\cos(z) + \left(1 - \lambda_k^2\cos^2(z)\right)^{\frac{1}{2}}\right), \tag{A.2}$$

$$h(z) = \frac{\pi}{2} - i\ln(\lambda_k) + i\ln\left(i\cos(z) + \left(\lambda_k^2 - \cos^2(z)\right)^{\frac{1}{2}}\right). \tag{A.3}$$

The orientation of the branch cuts depends exclusively on how we define $\left(1 - \lambda_k^2\cos^2(z)\right)^{\frac{1}{2}}$ and $\left(\lambda_k^2 - \cos^2(z)\right)^{\frac{1}{2}}$. To obtain the correct branch, we rewrite these in terms of sine instead of cosine and define each square root part separately. For $g(z)$, we define $\left(1 - \lambda_k^2\cos^2(z)\right)^{\frac{1}{2}}$ as,

$$\left(1 - \lambda_k^2\cos^2(z)\right)^{\frac{1}{2}} = -i\left(i\lambda_k\sin(z) - (1 - \lambda_k^2)^{\frac{1}{2}}\right)^{\frac{1}{2}}\left(i\lambda_k\sin(z) + (1 - \lambda_k^2)^{\frac{1}{2}}\right)^{\frac{1}{2}}, \tag{A.4}$$

such that,

$$\arg\left(i\lambda_k\sin(z) \pm (1 - \lambda_k^2)^{\frac{1}{2}}\right) \in (-\pi, \pi] \text{ and } \left(1 - \lambda_k^2\cos^2(z)\right)^{\frac{1}{2}}\Big|_{z=0} = (1 - \lambda_k^2)^{\frac{1}{2}}. \tag{A.5}$$

This definition is compared with the default one by comparing Figs A20a and A20c. We can define $h(z)$ in a similar way,

$$\left(\lambda_k^2 - \cos^2(z)\right)^{\frac{1}{2}} = \left(\sin(z) - (1 - \lambda_k^2)^{\frac{1}{2}}\right)^{\frac{1}{2}}\left(\sin(z) + (1 - \lambda_k^2)^{\frac{1}{2}}\right)^{\frac{1}{2}}, \tag{A.6}$$

where the two square roots are defined as follows:

$$\arg\left(\sin(z) \pm (1 - \lambda_k^2)^{\frac{1}{2}}\right) \in (-\pi, \pi] \text{ and } \left(\lambda_k^2 - \cos^2(z)\right)^{\frac{1}{2}}\Big|_{z=0} = i(1 - \lambda_k^2)^{\frac{1}{2}}. \tag{A.7}$$

This definition is compared with the default one by comparing Figs A20b and A20d.

However, Figs A20c and A20d show jumps across the infinite lines $\mathrm{Re}\{z\} = 2\pi n - \pi/2$ where $n \in \mathbb{Z}$. These jumps are of size 2π and appear because the default branch of $\ln(z)$ in MATLAB (and similar software) limits the imaginary part to $(-\pi, \pi]$. Logically, we can correct this issue to make $g(z)$ or $h(z)$ satisfy the condition $f(z + n\pi) = f(z) + n\pi$ by adding the following:

$$z - \frac{\pi}{2} - i\ln(ie^{-iz}) = 2\pi\left\lfloor\frac{\mathrm{Re}\{z\} + \pi/2}{2\pi}\right\rfloor = \begin{cases} \vdots & \\ -2\pi & -5\pi/2 \le \mathrm{Re}\{z\} < -\pi/2 \\ 0 & -\pi/2 \le \mathrm{Re}\{z\} < 3\pi/2 \\ 2\pi & 3\pi/2 \le \mathrm{Re}\{z\} < 7\pi/2 \\ \vdots & \end{cases} \tag{A.8}$$

Downloaded from https://academic.oup.com/imamat/article/85/3/421/5822762 by University of Cambridge user on 21 September 2020

to $g(z)$ and $h(z)$ where $\lfloor z \rfloor$ indicates the integer part. In the principal logarithm branch $\mathrm{Re}\left\{i\ln(ie^{-iz})\right\} \in (-\pi, \pi]$. This means our final definitions of $g(z)$ and $h(z)$ are,

$$g(z) = z - i\ln(ie^{-iz}) + i\ln\left(i\lambda_k\cos(z) - i\left(i\lambda_k\sin(z) - (1-\lambda_k^2)^{\frac{1}{2}}\right)^{\frac{1}{2}}\left(i\lambda_k\sin(z) + (1-\lambda_k^2)^{\frac{1}{2}}\right)^{\frac{1}{2}}\right) \quad \text{(A.9)}$$

$$h(z) = z - i\ln(ie^{-iz}) - i\ln(\lambda_k) + i\ln\left(i\cos(z) + \left(\sin(z) - (1-\lambda_k^2)^{\frac{1}{2}}\right)^{\frac{1}{2}}\left(\sin(z) + (1-\lambda_k^2)^{\frac{1}{2}}\right)^{\frac{1}{2}}\right). \quad \text{(A.10)}$$

Both these definitions satisfy all of the required conditions including the requirement that they are the inverse of each other. See Fig. 4 for an example phase plot illustration of (A.9) and (A.10) where $\lambda_k = 1/2$.

B. Asymptotic analysis of $q^{(0)}(z)$

In this appendix, we will discuss the asymptotic behaviour of the spectral function $q^{(0)}(z)$ as $|\mathrm{Im}\{z\}| \to \infty$. This could be useful because it can be pieced together with the asymptotic behaviour of the higher order spectral functions to find near-field approximations (as $kr \to 0$) or it can be used to improve the numerical methods present in Section 5.

It should be noted that the asymptotic expansion as $\mathrm{Im}\{z\} \to -\infty$ is the conjugate of the expansion as $\mathrm{Im}\{z\} \to \infty$ because $q^{(0)}(z^*) = \left(q^{(0)}(z)\right)^*$. For convenience, we shall restrict the wedge angle such that $\bar{\theta}_\mathrm{w} \le \theta_\mathrm{w}$ hence $\delta \le \bar{\delta}$. We shall write $q^{(0)}(z)$ as a half range real integral,

$$q^{(0)}(z) = \frac{i}{\pi}\int_0^\infty \frac{\bar{\delta}\sinh(\bar{\delta}\zeta)h'(i\zeta)s^{(0)}\left(\theta_\mathrm{w} + h(i\zeta)\right)}{\cosh(\bar{\delta}\zeta) + \sin(\bar{\delta}z)} - \frac{\bar{\delta}\sinh(\bar{\delta}\zeta)h'(i\zeta)s^{(0)}\left(-\theta_\mathrm{w} + h(i\zeta)\right)}{\cosh(\bar{\delta}\zeta) - \sin(\bar{\delta}z)}\mathrm{d}\zeta. \quad \text{(B.1)}$$

To find the asymptotic expansion of $q^{(0)}(z)$, we shall relate it to the following function:

$$I(y; a, b) = \int_0^\infty \frac{a\sinh(ax)f_+(x)}{\cosh(ax) + i\sinh(ay)} - \frac{a\sinh(ax)f_-(x)}{\cosh(ax) - i\sinh(ay)}\mathrm{d}x, \quad \text{(B.2)}$$

where $b \le a$ and $f_\pm(x)$ are complex functions that are well defined on the real line and have the following asymptotic expansions as $x \to \infty$:

$$f_\pm(x) = -ib \mp Ae^{-bx} + O(e^{-2bx}). \quad \text{(B.3)}$$

It is easy to see that $q^{(0)}(z) = \frac{i}{\pi}I(-iz; \bar{\delta}, \delta)$, $f_\pm(x) = h'(ix)s^{(0)}\left(\pm\theta_\mathrm{w} + h(ix)\right)$ and we want to find the asymptotic behaviour of (B.2) as $y \to \infty$. To do this, we need to split the integral as follows:

$$\int_0^\infty = \int_0^{\epsilon(y)} + \int_{\epsilon(y)}^\infty = I_1 + I_2,$$

Downloaded from https://academic.oup.com/imamat/article/85/3/421/5822762 by University of Cambridge user on 21 September 2020

where the midpoint $\epsilon(y)$ is designated so that $\epsilon(y) \to \infty$ and $\frac{\epsilon(y)}{y} \to 0$ as $y \to \infty$. We shall choose $\epsilon(y) = \frac{1}{a}\ln(y)$ and evaluate I_2 first. In this interval, x and y are considered to be very large and hence the integrand is approximated for large x and y,

$$I_2(y;a,b) = \int_{\epsilon(y)}^{\infty} \frac{a\sinh(ax)f_+(x)}{\cosh(ax)+i\sinh(ay)} - \frac{a\sinh(ax)f_-(x)}{\cosh(ax)-i\sinh(ay)}\mathrm{d}x,$$
$$\underset{y\to\infty}{\sim} -ib\int_{\epsilon(y)}^{\infty} \frac{ae^{ax}}{e^{ax}+ie^{ay}} - \frac{ae^{ax}}{e^{ax}-ie^{ay}}\mathrm{d}x - A\int_{\epsilon(y)}^{\infty} \frac{ae^{ax-bx}}{e^{ax}+ie^{ay}} + \frac{ae^{ax-bx}}{e^{ax}-ie^{ay}}\mathrm{d}x. \tag{B.4}$$

The first integral is trivial to integrate and the second can be integrated in terms of hypergeometric series (${}_2F_1$) by noting that,

$$\int \frac{x^{c-1}}{1-x}\mathrm{d}x = \sum_{n=0}^{\infty}\left(\int x^{c-1+n}\mathrm{d}x\right) = \frac{x^c}{c}\sum_{n=0}^{\infty}\left(\frac{cx^n}{c+n}\right) = \frac{x^c}{c}{}_2F_1(1,c;1+c;x).$$

Hence (B.4) is approximated as

$$I_2(y;a,b) \underset{y\to\infty}{\sim} -ib\ln\left(\frac{-1-iye^{-ay}}{1-iye^{-ay}}\right),$$
$$-\frac{aA}{b}y^{-\frac{b}{a}}\left({}_2F_1\left(1,\frac{b}{a};1+\frac{b}{a};-\frac{ie^{ay}}{y}\right)+{}_2F_1\left(1,\frac{b}{a};1+\frac{b}{a};\frac{ie^{ay}}{y}\right)\right).$$

We can find an asymptotic series for the hypergeometric function by using the following identity derived from equation 15.3.7 in Abramowitz & Stegun (1967),

$${}_2F_1(1,\sigma;1+\sigma;x) = \frac{\pi\sigma(-x)^{-\sigma}}{\sin(\pi\sigma)} - \frac{\sigma}{(\sigma-1)x}{}_2F_1(1,1-\sigma;2-\sigma;x^{-1}).$$

Hence the asymptotic expansions that we require are,

$$y^{-\frac{b}{a}}{}_2F_1\left(1,\frac{b}{a},1+\frac{b}{a},\mp\frac{ie^{ay}}{y}\right) = \frac{\pi b\,(\mp i)^{b/a}\,e^{-by}}{a\sin\left(\frac{\pi b}{a}\right)} \mp \frac{iby^{1-\frac{b}{a}}e^{-ay}}{(b-a)} + O(Y^{-2}).$$

After using the series expansions for hypergeometric series and for $\ln(1+z)$, we obtain the asymptotic approximation for I_2,

$$I_2(y;a,b) \underset{y\to\infty}{\sim} -\pi b + 2bye^{-ay} - \frac{\pi Ae^{-by}}{\sin\left(\frac{\pi b}{2a}\right)}. \tag{B.5}$$

Downloaded from https://academic.oup.com/imamat/article/85/3/421/5822762 by University of Cambridge user on 21 September 2020

For the other integral I_1, y is considered much larger than x, hence

$$I_1(y;a,b) = \int_0^{\epsilon(y)} \frac{a\sinh(ax)f_+(x)}{\cosh(ax)+i\sinh(ay)} - \frac{a\sinh(ax)f_-(x)}{\cosh(ax)-i\sinh(ay)}\mathrm{d}x,$$
$$\underset{y\to\infty}{\sim} \frac{-ia}{\sinh(ay)}\int_0^{\epsilon(y)} \sinh(ax)(f_+(x)+f_-(x))\mathrm{d}x. \tag{B.6}$$

We apply the following change of variables $x = \frac{1}{a}\ln(X)$:

$$I_1(y;a,b) \underset{y\to\infty}{\sim} \frac{1}{\sinh(ay)}\int_1^y \frac{1-X^{-2}}{2i}\left(f_+\left(\frac{1}{a}\ln(X)\right)+f_-\left(\frac{1}{a}\ln(X)\right)\right)\mathrm{d}X.$$

Recall (B.3) that implies that as $X\to\infty$,

$$f_+\left(\frac{1}{a}\ln(X)\right)+f_-\left(\frac{1}{a}\ln(X)\right) \underset{X\to\infty}{\sim} -2ib + O\left(X^{-\frac{2b}{a}}\right), \tag{B.7}$$

hence

$$I_1(y;a,b) \underset{y\to\infty}{\sim} -2b\left(y-2+\frac{1}{y}\right)e^{-ay}$$
$$+\frac{1}{\sinh(ay)}\int_1^y \frac{1-X^{-2}}{2i}\left(f_+\left(\frac{1}{a}\ln(X)\right)+f_-\left(\frac{1}{a}\ln(X)\right)+2ib\right)\mathrm{d}X.$$

The integral will be $o(y)$ as $y\to\infty$ because the integrand is well defined and bounded on the interval and is $o(1)$ as $X\to\infty$. This means that the leading order behaviour of $I_1(y;a,b)$ is,

$$I_1(y;a,b) = -2bye^{-ay} + o\left(ye^{-ay}\right). \tag{B.8}$$

So the asymptotic expansion for $I(y;a,b)$ as $y\to\infty$ is,

$$I(y;a,b) \underset{y\to\infty}{\sim} -\pi b - \frac{\pi A e^{-by}}{\sin\left(\frac{\pi b}{2a}\right)}. \tag{B.9}$$

Note that from the asymptotic expansions of $s^{(0)}(z)$, $h(z)$ and $h'(z)$, we can easily find that $A = 2i\delta\lambda_k^\delta\sin(\delta\theta_1)$, hence the asymptotic expansions for $q^{(0)}(z)$ as $\mathrm{Im}\{z\}\to\pm\infty$ are,

$$q^{(0)}(z) = \mp i\delta + \frac{2\delta\lambda_k^\delta\sin(\delta\theta_1)}{\sin(\delta\bar{\theta}_w)}e^{\pm i\delta z} + o(e^{\pm i\delta z}). \tag{B.10}$$

This same strategy can be applied to the higher order integrals as well but this is not discussed here for brevity.

Downloaded from https://academic.oup.com/imamat/article/85/3/421/5822762 by University of Cambridge user on 21 September 2020